

Robotic reverberation mapping of the broad-line radio galaxy 3C 120

Michael S. Hlabathe^{1b, 1,2★} David A. Starkey,³ Keith Horne,³ Encarni Romero-Colmenero,^{2,4}
Steven M. Crawford,⁵ Stefano Valenti,^{6,7} Hartmut Winkler,⁸ Aaron J. Barth^{1b, 9}, Christopher A. Onken^{1b, 10},
David J. Sand,¹¹ Tommaso Treu,¹² Aleksandar M. Diamond-Stanic¹³ and Carolin Villforth^{1b, 14}

¹University of Cape Town, Private Bag X3, Rondebosch 7701, South Africa

²South African Astronomical Observatory, PO Box 9, Observatory 7935, Cape Town, South Africa

³SUPA Physics and Astronomy, University of St Andrews, Fife, KY16 9SS, Scotland, UK

⁴Southern African Large Telescope Foundation, PO Box 9, Observatory 7935, Cape Town, South Africa

⁵Space Telescope Science Institute, 3700 San Martin Drive, Baltimore, MD 21218, USA

⁶Department of Physics, University of California, 1 Shields Avenue, Davis, CA 95616-5270, USA

⁷Las Cumbres Observatory Global Telescope Network, 6740 Cortona Drive, Suite 102, Goleta, CA 93117, USA

⁸Department of Physics, University of Johannesburg, PO Box 524, 2006 Auckland Park, South Africa

⁹Department of Physics and Astronomy, University of California, 4129 Frederick Reines Hall, Irvine, CA 92697-4575, USA

¹⁰Research School of Astronomy and Astrophysics, Australian National University, Canberra, ACT 2611, Australia

¹¹Department of Astronomy/Steward Observatory, 933 North Cherry Avenue, Room N204, Tucson, AZ 85721-0065, USA

¹²Department of Physics and Astronomy, University of California, Los Angeles, CA 90095-1547, USA

¹³Department of Physics and Astronomy, Bates College, 44 Campus Avenue, Lewiston, ME 04240, USA

¹⁴Department of Physics, University of Bath, Claverton Down Road, Bath BA2 7AY, UK

Accepted 2020 July 14. Received 2020 July 14; in original form 2019 November 5

ABSTRACT

We carried out photometric and spectroscopic observations of the well-studied broad-line radio galaxy 3C 120 with the Las Cumbres Observatory (LCO) global robotic telescope network from 2016 December to 2018 April as part of the LCO AGN Key Project on Reverberation Mapping of Accretion Flows. Here, we present both spectroscopic and photometric reverberation mapping results. We used the interpolated cross-correlation function to perform multiple-line lag measurements in 3C 120. We find the H γ , He II $\lambda 4686$, H β , and He I $\lambda 5876$ lags of $\tau_{\text{cen}} = 18.8^{+1.3}_{-1.0}$, $2.7^{+0.7}_{-0.8}$, $21.2^{+1.6}_{-1.0}$, and $16.9^{+0.9}_{-1.1}$ d, respectively, relative to the V-band continuum. Using the measured lag and rms velocity width of the H β emission line, we determine the mass of the black hole for 3C 120 to be $M = (6.3^{+0.5}_{-0.3}) \times 10^7 (f/5.5) M_{\odot}$. Our black hole mass measurement is consistent with similar previous studies on 3C 120, but with small uncertainties. In addition, velocity-resolved lags in 3C 120 show a symmetric pattern across the H β line, 25 d at line centre decreasing to 17 d in the line wings at $\pm 4000 \text{ km s}^{-1}$. We also investigate the inter-band continuum lags in 3C 120 and find that they are generally consistent with $\tau \propto \lambda^{4/3}$ as predicted from a geometrically thin, optically thick accretion disc. From the continuum lags, we measure the best-fitting value $\tau_0 = 3.5 \pm 0.2$ d at $\lambda_0 = 5477 \text{ \AA}$. It implies a disc size a factor of 1.6 times larger than prediction from the standard disc model with $L/L_{\text{Edd}} = 0.4$. This is consistent with previous studies in which larger than expected disc sizes were measured.

Key words: galaxies–Seyfert – quasars–galaxies – nuclei–galaxies – individual (3C 120) – galaxies – emission lines – supermassive black holes.

1 INTRODUCTION

It is believed that every active galactic nucleus (AGN) is powered by a supermassive black hole (BH) at its centre (Lynden-Bell & Rees 1971). For a detailed description of AGN and their different components, otherwise known as the unified model of an AGN, see Antonucci (1993) and Urry & Padovani (1995). The supermassive BHs in AGNs are believed to play a pivotal role in galaxy formation, thus encouraging efforts to understand their growth and distribution of mass over cosmological time.

In particular, the observed scaling relationships between BH mass M and host-galaxy properties, such as the velocity dispersion of the bulge stars ($M-\sigma_*$; Ferrarese & Merritt 2000; Gebhardt et al. 2000) or the bulge luminosity ($M-L_{\text{bulge}}$; Kormendy & Richstone 1995; Magorrian et al. 1998), indicate a strong connection between galaxy evolution and BH growth. To further investigate the nature of the BH–galaxy co-evolution, more BH masses must be accurately determined in both nearby galaxies and more distant AGNs. Dynamical methods based on high angular resolution kinematics of stars and gas have been widely used to measure masses of BHs in nearby galaxies (Kormendy & Gebhardt 2001; Ferrarese & Ford 2005). However, they are limited to the spatially resolved kinematics of nearby (few tens of Mpc) galaxies even with the current technology. Yet, in Type

★ E-mail: mh@sao.ac.za

1 AGNs, the broad emission lines from the broad-line region (BLR) can be used to probe the inner structure of the AGN and therefore determine M via a technique known as reverberation mapping (RM; Blandford & McKee 1982; Peterson 1993, 2001).

RM measures the mean time delay or lag τ between changes in the continuum from the accretion disc and corresponding changes in the broad emission lines, thus allowing for the direct measurement of the BLR size ($R_{\text{BLR}} = c\tau$) assuming light-traveltime effects. Typically, the time delay is found using traditional cross-correlation methods, such as the interpolation cross-correlation function (ICCF; Gaskell & Sparke 1986; Gaskell & Peterson 1987; White & Peterson 1994) or the discrete correlation function (Edelson & Krolik 1988). Over time, other approaches have been introduced for lag determination, such as Stochastic Process Estimation for AGN Reverberation (SPEAR and/or PYTHON implementation JAVELIN; Zu, Kochanek & Peterson 2011) and quite recently the Continuum REprocessed AGN Markov chain (CREAM; Starkey, Horne & Villforth 2016; Starkey et al. 2017), which have been found to perform better statistically on data with seasonal gaps or irregular sampling than the traditional methods (Grier et al. 2017b; Li et al. 2017).

By combining the measured τ and the velocity width ΔV [either from full width at half-maximum (FWHM) or line dispersion σ_{line}] of the broad emission line, and assuming virialized motions of the gas within the BLR, we can estimate the central BH mass as

$$M = f \frac{c \tau \Delta V^2}{G}, \quad (1)$$

where τ is the measured lag of the broad emission line, c is the speed of light, G is the gravitational constant, and f is a dimensionless factor that takes the structure, kinematics, and orientation effects of the BLR into account.

RM has been applied successfully in multiple spectroscopic campaigns, yielding >50 BH masses to date (e.g. Wandel, Peterson & Malkan 1999; Kaspi et al. 2000; Peterson et al. 2004; Bentz et al. 2009b; Denney et al. 2009a; Barth et al. 2011, 2015; Valenti et al. 2015; Shen et al. 2016; Fausnaugh et al. 2017; Du et al. 2018a; Grier et al. 2018; see also Bentz & Katz 2015). Although RM can be used to find BH masses in nearby and distant AGNs, it does, however, require long-term monitoring, high cadence and signal-to-noise, which is observationally hard to achieve using ground-based telescopes. Fortunately, RM also provides a scaling relationship between BLR size and the AGN luminosity at 5100 Å ($R_{\text{BLR}}-L_{5100}$; e.g. Bentz et al. 2013), thus allowing for the measurement of BH mass using single-epoch spectrum of the AGN (e.g. Wandel et al. 1999; Vestergaard 2002).

RM can also be used to provide some insight into the structure and size of the accretion disc in AGN using the wavelength-dependent continuum delays, wherein ionizing photons from a compact region near BH propagate outwards and are reprocessed into UV/optical continuum emission with light-traveltime delays that increase with wavelength (e.g. Cackett, Horne & Winkler 2007). By measuring the continuum time delay τ as a function of wavelength λ , RM can probe the radial temperature profile of the accretion disc and test the $\tau \propto \lambda^{4/3}$ prediction of the standard thin-disc model of Shakura & Sunyaev (1973).

Here, we undertake a robotic RM study of 3C 120 (Table 1) from long-term monitoring with the Las Cumbres Observatory (LCO) global robotic telescope network. 3C 120 was shown to exhibit a type 1 Seyfert spectrum by Sargent (1967) and it was one of the first radio sources for which variability was confirmed (Pauliny-Toth & Kellermann 1966). Furthermore, 3C 120 became the subject of much

Table 1. Object properties.

Object	RA ^a (J2000)	Dec ^a (J2000)	D_L^b (Mpc)	z^a
3C 120	04 33 11.1	+05 21 16	139	0.0330

Notes. ^aValues from the NED data base.

^bAdopted luminosity distance for our cosmological model.

interest when the apparent superluminal motion of its radio jet was discovered (Walker 1997; Gómez et al. 2011).

3C 120 has also been the subject of several previous reverberation studies over the years. Observational campaigns in the late 1990's (Peterson et al. 1998b), later reanalysed by Peterson et al. (2004), determined a time lag of ~ 40 d between the continuum and the H β line. Kollatschny et al. (2014) performed a reverberation analysis of a set of 3C 120 optical spectra secured between 2008 September and 2009 March, concluding that the H β lag relative to the continuum is $27.9^{+7.1}_{-5.9}$ d. Du et al. (2018b) determined the H β -to-continuum delay to be $20.2^{+5.0}_{-4.2}$ d. 3C 120 has also been the subject of infrared dust RM by Ramolla et al. (2018). Using our high signal-to-noise observations, we aim to accurately determine M in 3C 120 along with measuring the inter-band continuum lags.

We arranged this paper as follows: In Section 2, we describe the observations and data reduction. Section 3 reviews the time-series analysis methodology. Section 4 presents the inter-band continuum delays in context with the standard accretion-disc theory. Section 5 presents the BH mass measurements. In Section 6, we investigate the structure and kinematics of the BLR in 3C 120. We discuss our results and summarize our conclusions in Sections 7 and 8, respectively. We assumed a cosmological model with $H_0 = 73.0 \text{ km s}^{-1} \text{ Mpc}^{-1}$, $\Omega_m = 0.27$, and $\Omega_\Lambda = 0.73$.

2 OBSERVATIONS AND DATA REDUCTION

To carry out an RM analysis on 3C 120, we require continuum light curve(s) that we measure from photometry and emission-line light curve(s) from spectroscopy. The data employed here were acquired as part of the LCO AGN Key Project titled Reverberation Mapping of AGN Accretion Flows (Valenti et al. 2015). The observations include 6-band photometric imaging (Section 2.1) and FLOYDS spectroscopy (Section 2.2).

2.1 Photometry

Our photometric monitoring campaign of 3C 120 in 6 bands (U , g' , V , r' , i' , z_s) ran from 2016 December to 2018 April using the LCO 1m robotic telescopes (Brown et al. 2013) deployed at Siding Spring Observatory (SSO), South African Astronomical Observatory (SAAO), McDonald Observatory (McD), and Cerro Tololo Interamerican Observatory (CTIO). A journal of photometric observations is presented in Table 2, and the resulting light curves in Fig. 2. All observations were taken with Sinistro, a 4k×4k-pixel quad-readout CCD camera with a 26.5×26.5 arcmin field of view and a pixel scale of $0.389 \text{ arcsec pixel}^{-1}$. We obtained 563 observations in the Johnson V filter, 432 in the Johnson U filter, 508 in the SDSS g' filter, 498 in the SDSS r' filter, 480 in the SDSS i' filter, and 460 in the Pan-STARRS z_s filter with nearly daily cadence during 50 nights before and 250 nights after the 100 d solar conjunction gap.

The basic data reduction steps were carried out using the LCO BANZAI data pipeline (Brown et al. 2013), which performs flat-fielding and bias subtraction. Subsequent to this, all images were

Table 2. Summary of photometric observations for 3C 120.

Filter ^a	λ_{pivot}^b	LCO site ^c	Date range ^d	t_{exp} (s)	Epochs ^e	Total ^f
<i>U</i>	3656 Å	SAAO	20170826–20180327	300	107	432
		McD	20170810–20180315		14	
		SSO	20170806–20180207		90	
		CTIO	20170804–20180406		221	
<i>g'</i>	4770 Å	SAAO	20170306–20180327	120	149	508
		McD	20170330–20180315		14	
		SSO	20170306–20180207		91	
		CTIO	20170309–20180406		254	
<i>V</i>	5477 Å	SAAO	20170106–20180327	300	156	563
		McD	20170330–20180315		14	
		SSO	20161228–20180207		113	
		CTIO	20170106–20180406		280	
<i>r'</i>	6231 Å	SAAO	20170308–20180406	120	171	498
		McD	20170405–20180306		12	
		SSO	20170306–20180404		125	
		CTIO	20170314–20180409		190	
<i>i'</i>	7625 Å	SAAO	20170308–20180406	120	158	480
		McD	20170405–20180306		12	
		SSO	20170306–20180404		124	
		CTIO	20170314–20180309		186	
<i>z_s</i>	8660 Å	SAAO	20170308–20180406	240	160	460
		McD	20170405–20180306		11	
		SSO	20170306–20180304		106	
		CTIO	20170314–20180409		183	

Notes. ^aThe filter through which the data were taken.

^bFilter centroid wavelength.

^cSAAO, McD, SSO, and CTIO.

^dStart and end date of observations; we note the ~ 100 d gap due to solar conjunction.

^eThe number of observations taken in that date range per filter.

^fThe total number of observations taken in that filter from all telescopes combined.

cleaned of cosmic rays applying the L.A.Cosmic algorithm (van Dokkum 2001).

To construct differential light curves in the respective bands, we performed a multi-aperture photometry in AstroImageJ. AstroImageJ is an image analysis tool designed to automatically go through a set of time-series images and measure light curves (Collins et al. 2017).

We analysed the data set from each filter separately but in the same manner. First, we aligned the *V* images using *Align stack using WCS* functionality in AstroImageJ. Using visual inspection, we selected from a set of aligned images, one of the images with the best seeing. We selected five comparison stars on the basis of their brightness and relative isolation (Fig. 1). We then measured the FWHM in pixels of those stars using *Plot seeing profile* in AstroImageJ, and recorded the measurements. Next, we randomly selected 20 more images from the set and measured the FWHM of the comparison stars. We then combined all the measured FWHMs to produce the average. Using the average value, an aperture radius and sky annulus radii were then determined as recommended in Collins et al. (2017). This resulted in an aperture radius of 12 pixels (5.0 arcsec) and inner and outer sky aperture radii of 22 and 33 pixels, respectively. We adopted the same aperture and sky annulus radii for all filters.

AstroImageJ produces a measurement table that includes among other parameters sky-subtracted counts of the target and that of the chosen comparison stars. To perform differential photometry, we measure instrumental magnitudes of the target and comparison stars from the measured counts. We then selected a reference frame (first image in the set) as the zero-point. We calculated the magnitude

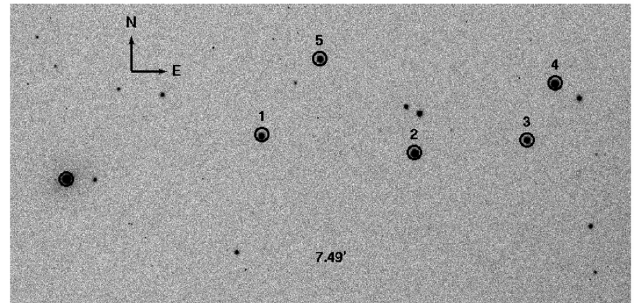


Figure 1. A cut-out of the full Sinistro *V*-band image of 3C 120 taken with the CTIO 1m telescope. The comparison stars used in the differential photometry are indicated. Image is 7.49 arcmin across; the N and E pointers/arrows are 0.3 arcmin in length.

difference (Δm) of each comparison star between the reference epoch and each epoch. We also calculated the rms variability of each comparison star based on the resulting Δm . The comparison star with lowest rms variability was selected as the main comparison star and others as check stars. For each filter, a different comparison star was selected as indicated in Table 3. We subtracted the main comparison star from the check stars ($\Delta m - \Delta m_{\text{comp}}$). As a consistency check, we found the check stars to yield rms intrinsic variations of about 1 per cent. We then also subtracted the main comparison star from the target to get the differential magnitudes of the target

Table 3. The comparison star AB magnitudes for each filter.

Filter	Comp 1	Comp 2	Comp 3	Comp 4	Comp 5
<i>U</i>	16.5 ± 0.2 ^a	16.3 ± 0.2	17.5 ± 0.2	16.8 ± 0.2	17.6 ± 0.2
<i>g'</i>	15.737 ± 0.076 ^a	14.994 ± 0.024	15.881 ± 0.081	15.071 ± 0.05	15.918 ± 0.049
<i>V</i>	15.388 ± 0.058	14.480 ± 0.019 ^a	15.417 ± 0.035	14.449 ± 0.044	15.424 ± 0.031
<i>r'</i>	15.182 ± 0.047 ^a	14.162 ± 0.063	14.962 ± 0.077	14.014 ± 0.041	15.110 ± 0.042
<i>i'</i>	14.89 ± 0.06	13.86 ± 0.04	14.58 ± 0.04 ^a	13.54 ± 0.06	14.8 ± 0.1
<i>z_s</i>	–	13.7374 ± 0.0033 ^a	14.4569 ± 0.0044	13.3687 ± 0.0005	14.6546 ± 0.0057

Note. ^aComparison stars used in the calibration.

($m_{\text{target}} - m_{\text{comp}}$). We calibrated the differential magnitudes of the target using the catalogue (APASS; Henden et al. 2015) and (Pan-STARRS; Chambers et al. 2016) magnitudes of the comparison stars. As a reference *U*-band magnitude could not be found for the comparison stars, we estimate the *U*-band flux for the comparison stars based on the *B*–*V*, *U*–*B* colours (Fitzgerald 1970; Ducati et al. 2001) and assuming a 0.2 mag uncertainty on the resulting *U* magnitude. We then performed a conversion to AB system for Johnson *U* and *V* magnitudes (Blanton & Roweis 2007). Finally, we flux-calibrated the differential light curve of the target to mJy. The same procedure was repeated for each filter. In Table 3, we give the adopted mean AB magnitude and its uncertainty for each comparison star.

In the resulting light curves, we removed extreme outliers (verified by inspection of the images to be caused by, for example, cosmic ray hits, bad CCD pixels, strong sky gradients, clouds, etc.). This left us with 541 (96 per cent) data points on the final light curve in *V*, 380 (88 per cent) in *U*, 476 (94 per cent) in *g'*, 446 (90 per cent) in *r'*, 439 (92 per cent) in *i'*, and 425 (92 per cent) in *z_s*. We present the resulting 3C 120 light curves in each band in Fig. 2 and Table A1. The light curves exhibit strong variations with similar structure across all the photometric bands. Several 10–20 per cent features on 30–100 d time-scales are detected with high S/N, as well as numerous smaller features. These well-detected variations provide the basis for measuring inter-band time delays. We also note that there may be potential emission-line contamination of the broadband photometric light curves, which could later impact the measured time lags between the bands.

2.2 Spectroscopy

The spectroscopic observations were acquired robotically with the FLOYDS spectrographs between 2017 March and 2018 March. The FLOYDS spectrographs are two almost identical spectrographs on the LCO 2m telescopes, the Faulkes Telescope North (FTN) at Haleakela, Hawaii, and South (FTS) at Siding Springs in Australia. The spectrographs cover concurrently a wavelength range of 4800–10 000 Å in first order and 3200–5900 Å in second order. The pixel scales are 3.51 Å pixel^{−1} in first order and 1.74 Å pixel^{−1} in second order, which corresponds to resolutions of 17 and 9 Å using a slit width of 2 arcsec, respectively. For brevity, these will be referred to as the red and blue sides, respectively. We acquired a total of 149 spectroscopic epochs at a median sampling of 2 d. Spectra were taken in pairs with 1800 s per spectrum.

The data were reduced separately for the blue and red sides using the AGN FLOYDS pipeline written in PYRAF/PYTHON.¹ The pipeline includes overscan subtraction, flat-fielding, defringing, cosmic ray

rejection using the L.A.Cosmic algorithm (van Dokkum 2001), order rectification, spectral extraction, flux, and wavelength calibration. All these steps were performed without human interaction.

We inspected the resulting 1D spectra visually and we discarded the bad spectra, either due to significantly poor S/N or the pipeline failing to extract the 1D spectra. Doing this procedure, we ended up with 128 blue spectra (97 FTN, 31 FTS) and 137 red spectra (98 FTN, 39 FTS). Since the H β emission line is observed in both orders (red and blue), it permits for simultaneous measurements of the line providing a way to cross-check our measurements (Valenti et al. 2015).

We analysed separately the blue and red spectra, and further divided the FTN and FTS spectra, which have slightly different wavelength scales and flux calibrations. We also exclude the H α line from further analysis as it is affected by fringing.

2.3 Spectral modelling with PrepSpec

To extract the emission-line light curves, we employ a multi-epoch spectral fitting tool called PrepSpec (Shen et al. 2015, 2016). PrepSpec was written in FORTRAN by K. Horne and is optimized to perform simultaneous spectral fitting of AGN spectra. We analyse spectra from the blue and red sides separately. For a full description of PrepSpec, see Shen et al. (2016).

To mitigate flux calibration errors due to slit losses and changes in atmospheric transparency, PrepSpec fits a model to the input spectra defined as

$$\mu(t, \lambda) = p(t)[A(\lambda) + B(t, \lambda) + C(t, \lambda)], \quad (2)$$

where $A(\lambda)$ is the average spectrum, $B(t, \lambda)$ is the variable BLR, and $C(t, \lambda)$ is the variable continuum. $p(t)$ are the time-dependent photometric corrections determined by assuming that the narrow emission-line ([O III] λλ4959, 5007 and other) fluxes remain constant throughout the RM monitoring period. Even though narrow emission lines have been found to vary over long time-scales (~several years; Peterson et al. 2013), this assumption is valid for short time-scales (days to months). The variable BLR is modelled as a sum over lines of the line profile multiplied by the line light curve,

$$B(t, \lambda) = \sum_{\ell=1}^{N_{\ell}} B_{\ell}(\lambda) L_{\ell}(t). \quad (3)$$

Here $\langle L \rangle = 0$ and $\langle L^2 \rangle = 1$ to resolve the degeneracy between $B_{\ell}(\lambda)$ and $L_{\ell}(t)$, so that the rms profile of the line ℓ is $B_{\ell}(\lambda)$. The light curve of the line ℓ is $L_{\ell}(t)$ multiplied by the integral of the line flux in the rms spectrum

$$B_{\ell}(t) = L_{\ell}(t) \int B_{\ell}(\lambda) d\lambda. \quad (4)$$

The average spectrum $A(\lambda)$ is the sum of the broad-line, continuum,

¹https://github.com/svalenti/FLOYDS_pipeline.git

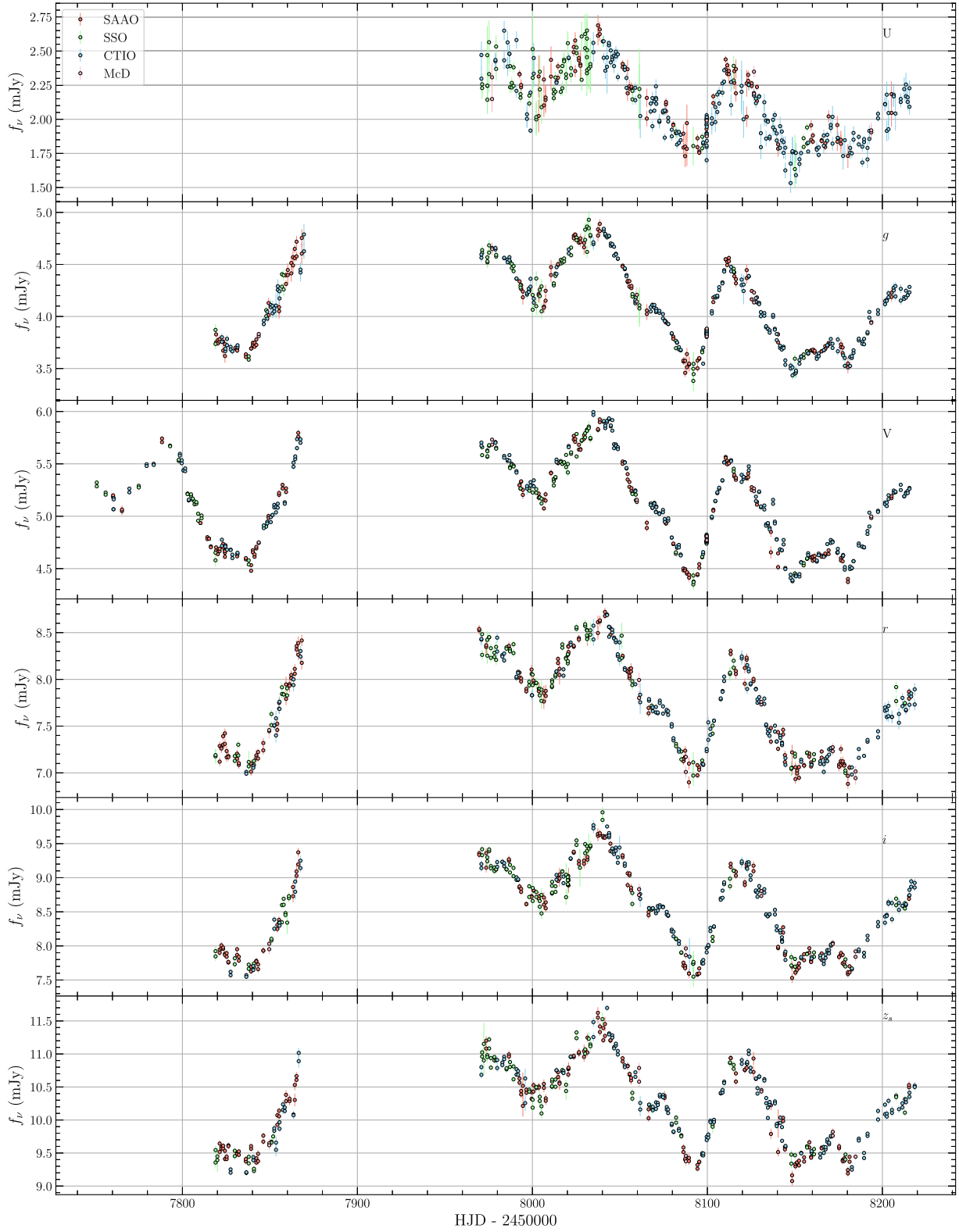


Figure 2. The 3C 120 continuum light curves in (top to bottom) U , g' , V , r' , i' , and z_s . Data are ordered by wavelength.

and narrow-line components. Mathematically,

$$A(\lambda) = \bar{F}(\lambda) + N(\lambda).$$

(5)

In this case, $\bar{F}(\lambda)$ encapsulates both the broad-line and continuum components, and $N(\lambda)$ is the narrow-line component. Unlike many RM studies in which a power law is used to model the changes in the continuum, PrepSpec uses a low-order polynomial in $\log \lambda$ with

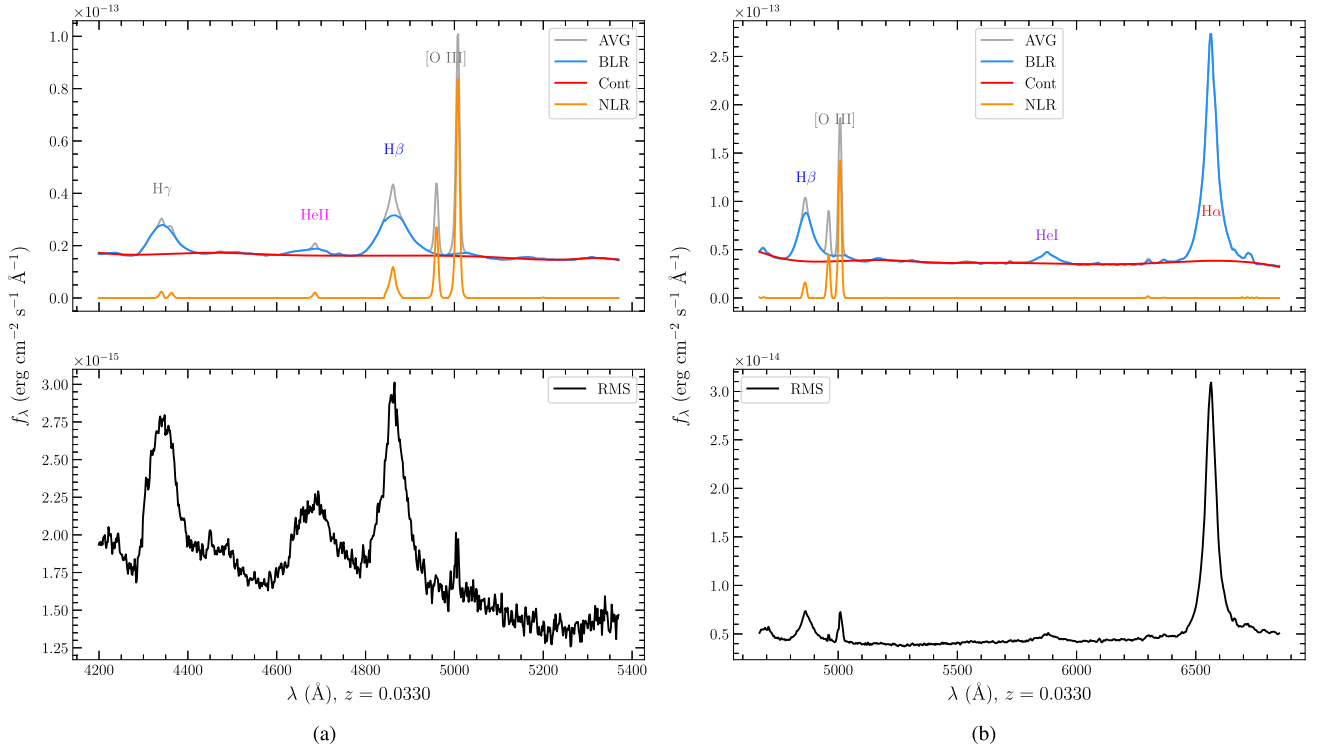


Figure 3. (Left) Mean (top) and rms (bottom) spectrum of 3C 120 from the FTN data (blue side), which includes 97 epochs. Labelled are $H\gamma$ $\lambda 4340$, $He II$ $\lambda 4686$, $H\beta$ $\lambda 4861$, and $[O III]$ $\lambda\lambda 4959, 5007$ emission lines. (Right) Mean (top) and rms (bottom) spectrum of 3C 120 from the FTN data (red-side), which includes 98 epochs. Labelled are $H\beta$ $\lambda 4861$, $[O III]$ $\lambda\lambda 4959, 5007$, and $He I$ $\lambda 5876$ emission lines. The $H\alpha$ line is excluded from our time-series analysis due to it being affected by fringing.

time-dependent coefficients to model the variations in the continuum $C(t, \lambda)$. PrepSpec also includes small corrections taking into account spectral blurring due to seeing and small wavelength shifts due to instrument flexure and differential refraction.

PrepSpec optimizes the model parameters to fit all spectra simultaneously. PrepSpec outputs the mean and root-mean-square (rms) residual line profiles (Fig. 3). The mean spectra exhibit strong narrow $[O III]$ emission lines, with weaker narrow-line components on the $H\gamma$, $H\beta$, $He II$ $\lambda 4686$, and $He I$ $\lambda 5876$ lines. The PrepSpec model uses all of these narrow features to define the calibration tweaks. The blue and red spectra both cover $H\beta$ and $[O III]$, providing two independent measures of the $H\beta$ line profile and variations. The continuum is roughly flat in the mean f_λ spectrum and significantly bluer in the rms spectrum. The broad emission lines are more prominent in the rms than in the mean spectrum, particularly for $He II$ $\lambda 4686$.

PrepSpec also produces measurements of the integrated broad emission-line fluxes (Fig. 4 and Table A2), linewidth measurements (FWHM, σ_{line}), and their statistical errors for each of the broad lines. The measured linewidths are listed in Table 4 for comparison. The highly ionized $He II$ $\lambda 4686$ line exhibits broader linewidth in the rms spectrum due to its close origin to the ionizing source. Generally, we measure small uncertainties on the linewidths due to high S/N of our data. However, we do note that because of the ambiguity in separating the NLR and BLR components, and placing the continuum, the measured linewidths may be over/underestimated.

Correlated variations across all the emission lines are seen in Fig. 4. The $He II$ $\lambda 4686$ variations track the V-band variations quite closely, while $He I$ $\lambda 5876$ and the Balmer line variations exhibit evidence for a more substantial lag, despite their relatively large scatter around

HJD-2450000 = 8100–8150. For example, the V-band light curve rises from 8090–8110 and then falls until 8150. In this same time interval, $He II$ rises and falls similarly to V while the Balmer and $He I$ rise and flatten off. Near 8020–8030, the $He II$ $\lambda 4686$, $He I$ $\lambda 5876$, and Balmer line fluxes seem low compared with the relatively high V-band flux. This suggests that long-term trends may differ between lines and continuum, thus potentially affecting lag measurements based on the faster variations.

3 TIME-SERIES ANALYSIS

3.1 Variability amplitudes

We characterize the variability of each light curve by measuring the fractional rms amplitude, F_{var} , defined as

$$F_{var} = \frac{\sqrt{\sigma_\ell^2 - \delta_{rms}^2}}{\langle \ell \rangle}, \quad (6)$$

where $\langle \ell \rangle$ and σ_ℓ^2 are the mean and variance of the light curve, respectively, and δ_{rms}^2 is the rms uncertainty on the measured fluxes (Rodríguez-Pascual et al. 1997; Edelson et al. 2002). The calculated F_{var} and its uncertainty for each broad emission-line light curve are tabulated in Table 5. The variability amplitude of about 10 per cent is considered adequate for reverberation studies (Rodríguez-Pascual et al. 1997). $He II$ $\lambda 4686$ exhibits substantial (30 per cent rms) variability. Correlated variations are evident in the Balmer and $He I$ light curves despite their lower fractional variations (~ 8 –11 per cent). We also calculate F_{var} for the continuum light curves (Fig. 2) and list the results in Table 7. We generally find F_{var} values that decrease with increasing wavelength likely due to the variable component of

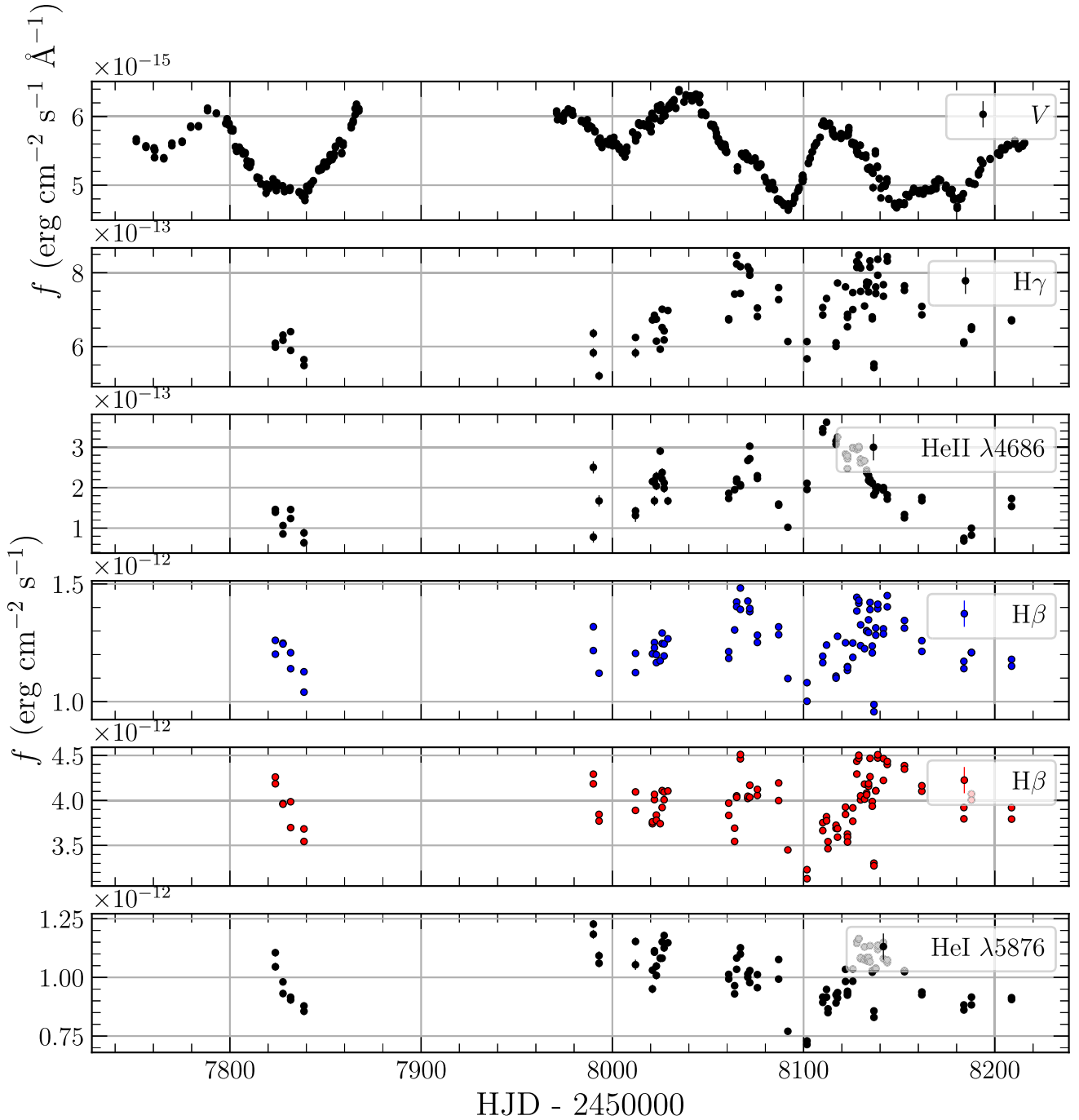


Figure 4. V-band continuum and broad emission-line ($H\gamma$ $\lambda 4340$, $He II$ $\lambda 4686$, $H\beta$ $\lambda 4861$, $He I$ $\lambda 5876$) light curves from PrepSpec using the FTN data.

Table 4. Emission-line widths in the mean and rms spectra.

Line	FWHM (mean) (km s ⁻¹)	FWHM (rms) (km s ⁻¹)	σ_{line} (mean) (km s ⁻¹)	σ_{line} (rms) (km s ⁻¹)	Window (Å)
$H\gamma$	4402 \pm 5	4469 \pm 14	1703 \pm 1	1786 \pm 3	4270–4415
$He II$ $\lambda 4686$	5271 \pm 20	6592 \pm 26	2007 \pm 4	2282 \pm 2	4609–4766
$H\beta$ blue side	4754 \pm 4	3273 \pm 8	1923 \pm 1	1657 \pm 3	4782–4944
$H\beta$ red side	4412 \pm 5	3874 \pm 12	2002 \pm 1	1810 \pm 3	4782–4944
$He I$ $\lambda 5876$	3948 \pm 11	4408 \pm 30	2044 \pm 4	2037 \pm 12	5751–6006

Table 5. 3C 120 broad emission-line lags relative to V .

Line curve	r_{\max}	τ_{cent} (days)	$\tau_{\text{CREAM}} - \tau_V$ (days)	F_{var}
H γ	0.28	$18.8^{+1.3}_{-1.0}$	17.6 ± 1.3	0.110 ± 0.008
He II	0.53	$2.7^{+0.7}_{-0.8}$	3.0 ± 0.7	0.296 ± 0.022
H β blue side	0.42	$21.2^{+1.6}_{-1.0}$	19.4 ± 1.7	0.083 ± 0.006
H β red side	0.38	$21.2^{+1.6}_{-1.0}$	20.2 ± 2.4	0.089 ± 0.006
He I	0.69	$16.9^{+0.9}_{-1.1}$	16.6 ± 1.3	0.102 ± 0.007

Note. $\tau_V = 2.26 \pm 0.18$ d.

the light from the accretion disc being bluer than the non-variable components, such as host-galaxy starlight with the exception of the i' band.

3.2 Cross-correlation analysis

To estimate the time delay τ of the broad emission lines (H γ , He II, H β , He I) relative to the continuum light curve, we used the ICCF (Gaskell & Sparke 1986; Gaskell & Peterson 1987; White & Peterson 1994) method. We cross-correlated the emission-line light curves (Fig. 4) with the V -band continuum light curve (Fig. 2). We chose the V -band continuum light curve because it has more observations and better S/N than the other continuum light curves in Fig. 2.

For two light curves $x(t)$ and $y(t)$ sampled at times t_i , the cross-correlation function ICCF (τ) is given by

$$\text{ICCF}(\tau) = \frac{1}{N} \frac{\sum_i (x(t_i) - \bar{x})(y(t_i - \tau) - \bar{y})}{\sigma_y \sigma_x}, \quad (7)$$

where \bar{x} and σ_x are, respectively, the mean and standard deviation of the N light-curve samples $x(t_i)$, and similarly for y . In the ICCF, the cross-correlation coefficient is calculated twice. First, by cross-correlating the original continuum light curve $y(t_i)$ with the linearly interpolated emission-line light curve $x(t_i - \tau)$ for a given lag τ . Secondly, by cross-correlating the linearly interpolated continuum light curve $y(t_i - \tau)$ with the original emission-line light curve $x(t_i)$ for a given lag. The ICCF (τ) is then taken to be the mean of the two results. We explored a time lag range from -10 to 50 d using the interpolation grid spacing of 0.25 d. We based our measured lags on the ICCF centroid (τ_{cen}) calculated using all r values above a threshold $r > 0.8r_{\max}$ (Peterson et al. 2004), where r_{\max} is the maximum value of the correlation coefficient.

Uncertainties on the measured lags were determined using the flux randomization and random subset selection method (FR/RSS; Peterson et al. 1998a) in the form of PyCCF² (Sun, Grier & Peterson 2018). For each realization or iteration, individual points are sampled randomly from the original set with replacement, thus resulting in some of the points being excluded and others being selected more than once. In the resulting set, the duplicate points are ignored, which then reduces the set to typically ~ 37 per cent of the original set. The remaining points are then perturbed by adding random Gaussian deviates based on the associated error and each time calculating τ_{cen} . This procedure was repeated 10^3 times to build up a cross-correlation centroid distribution (CCCD; Fig. 5) that yielded the median lag and the 68 per cent confidence interval.

In our ICCF analysis, we omit the FTS data. When using both FTS and FTN spectra, which have slightly different wavelength scales and flux calibrations, the resulting merged emission-line light curves had

small but significant jumps between the FTN and FTS data points. This adversely affected the ICCF analysis. Therefore, we opted to use just the FTN spectra, which had better time sampling than FTS. We summarize the resulting ICCF lag measurements in Table 5 (and Fig. 5). The FTN blue and red spectra give consistent H β lag measurements with $21.2^{+1.6}_{-1.0}$ and $21.2^{+1.6}_{-1.0}$ d, respectively, indicating that our emission-line flux measurements are reliable. The H γ lag ($18.8^{+1.3}_{-1.0}$) is consistent with the H β measurements. The He lines, He II $\lambda 4686$ lag ($2.7^{+0.7}_{-0.8}$) and He I $\lambda 5876$ lag ($16.9^{+0.9}_{-1.1}$), have shorter delays than the Balmer lines. Generally, we measure r_{\max} values that are lower for each of the broad lines despite the ICCF being well behaved. 3C 120 being a radio galaxy (also a miniblazar), there may be an additional contribution by the optical synchrotron continuum emission from the jet that could affect the correlation coefficient values (Li et al. 2020; Zhang et al. 2019). However, synchrotron emission would introduce features in the continuum light curve, and the low correlation coefficients we see stem from relatively large scatter in the emission-line (particularly H γ and H β) data that are not present in the V continuum light curve. We believe that this scatter arises from limitations in the accuracy of our spectrophotometric calibration, rather than to variable jet emission affecting the light curves. To try to improve the coefficients, we applied detrending (Welsh 1999) prior to ICCF analysis. We then omitted the pre-gap spectra with/without detrending. In all cases, the ICCF results did not improve considerably.

In addition to the broad emission-line lags with ICCF, we measure the lag between the continuum bands with respect to V in a similar manner as above (Table 7). We give more emphasis on the outcome and implications in terms of the standard disc model in Section 4.

3.3 CREAM modelling

We undertook a separate analysis of the light curves in addition to the ICCF, using the Continuum REprocessed AGN Markov chain Monte Carlo code (CREAM; Starkey et al. 2016)³ with the aim of comparing the results with the ICCF. The ICCF method works best with regularly sampled data and accurate uncertainty estimates, while CREAM fits a parametrized model to the light-curve data, including parameters for the reverberating disc model and a noise model, with one or two parameters per light curve that adjusts the nominal error bars. The noise model optimizes an additive extra variance parameter (σ_0^2) and multiplicative error-bar scaling factor (e) such that

$$\sigma_{\text{new}} = \sqrt{(e\sigma_{\text{old}})^2 + \sigma_0^2}. \quad (8)$$

For the CREAM analysis, we model both the FTN and FTS data simultaneously. CREAM fits a lampost model with driving light curve $X(t)$ to the input continuum light curves $f_v(\lambda, t)$ with the continuum response function $\psi(\tau|\lambda)$,

$$f_v(\lambda, t) = \bar{F}_v(\lambda) + \Delta F_v(\lambda) \int X(t - \tau) \psi(\tau|\lambda) d\tau, \quad (9)$$

in order to infer the shape of the true driving light curve that drives the continuum variability. The driving light curve $X(t)$ is normalized to $\langle X \rangle = 0$ and $\langle X^2 \rangle = 1$, so that $\bar{F}_v(\lambda)$ and $\Delta F_v(\lambda)$ represent the mean and rms spectra, respectively. The continuum response function is normalized to $\int \psi(\tau|\lambda) d\tau = 1$. For the continuum delay distribution, we adopt a face-on (inclination $i = 0$) steady-state

²https://bitbucket.org/cgrier/python_ccf_code

³Python version from <https://github.com/dstarkey23/pyccream>

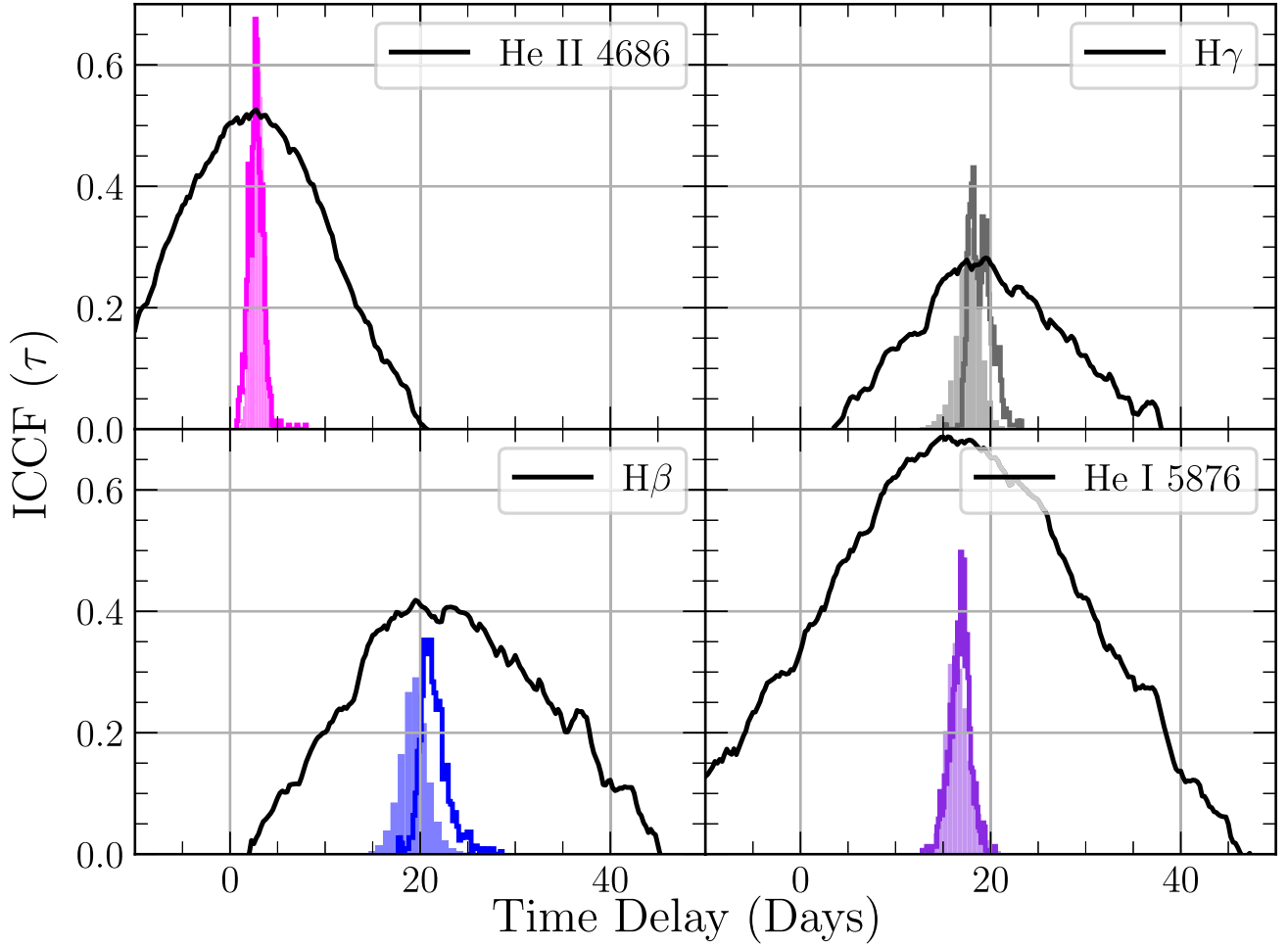


Figure 5. The solid lines are the ICCFs $r(\tau)$, and corresponding CCCDs are defined by the FR/RSS samples (solid line histograms). The translucent histograms are the posterior delay distributions (also shown in Fig. 7 panels a–e) defined by CREAM’s MCMC samples of the mean delay of top-hat response functions. These results are only for FTN spectra.

blackbody accretion disc with a power-law temperature profile

$$T = T_1 \left(\frac{r}{r_1} \right)^{-\alpha}, \quad (10)$$

where T_1 is the temperature at $r_1 = 1$ light day and $T \propto r^{-\alpha}$ corresponds to $\tau \propto \lambda^{1/\alpha}$. For the steady disc model, $\alpha = 3/4$ and $\tau \propto \lambda^{4/3}$ and

$$T_1^4 = \frac{3 G M \dot{M}}{8 \pi \sigma r_1^3}, \quad (11)$$

for a given BH mass M and mass accretion rate \dot{M} . Thus, $\tau(\lambda)$ tests the prediction $\alpha = 3/4$ and T_1 then measures the product $M \dot{M}$.

CREAM assumes that the origin of accretion-disc variability is a centrally located point source with a stochastic luminosity modelled as a time series $X(t)$ given by

$$X(t) = \sum_{k=1}^{N_k} C_k \cos(\omega_k t) + S_k \sin(\omega_k t), \quad (12)$$

where $\omega_k \equiv k \Delta\omega$ are equally spaced Fourier frequencies, with C_k and S_k the corresponding Fourier amplitudes that describe the shape of the lamppost light-curve variations. To incorporate prior knowledge about the character of AGN light curves, CREAM includes priors on the S_k and C_k parameters that steer the power

spectrum of the driving light curve towards a random walk, with Fourier power-density spectrum $P(\omega) \propto \omega^{-2}$. These random walk priors are Gaussian with mean $\langle S_k \rangle = \langle C_k \rangle = 0$ and standard deviation σ_k , where

$$\sigma_k^2 = \langle S_k^2 \rangle + \langle C_k^2 \rangle = P(\omega_k) \Delta\omega = P_0 \Delta\omega \left(\frac{\omega_0}{\omega_k} \right)^2. \quad (13)$$

CREAM’s fitted parameters and their priors are summarized in Table 6.

Following Grier et al. (2017b), we use CREAM to fit multiple continuum light curves simultaneously with multiple emission-line light curves. For each line, we adopt a uniform (top-hat) delay distribution specified by mean delay $\bar{\tau}$ and delay width $\Delta\tau$. This is based on the assumption that the BLR responds to changes by the driving light curve. CREAM treats the emission-line light curves as delayed and smoothed versions of the inferred driving light curve with a top-hat response function similar to that used in JAVELIN (Zu et al. 2011). CREAM estimates parameter uncertainties using a Markov chain, in our case with 10^5 samples.

In modelling the light curves, we fit only the temperature T_1 at 1 light day from the BH, holding the power-law index $\alpha \equiv 3/4$ and face-on inclination $i = 0$. We used our derived BH mass $M = 6.3 \times 10^7 M_\odot$ (Section 5) for consistency. We also set the upper

Table 6. Summary of priors on each of the CREAM parameters.

Parameter	N_{par}	Prior
S_k and C_k	$2N_k$	Gaussian ($\langle S_k \rangle = \langle C_k \rangle = 0$, $\langle S_k^2 \rangle = \langle C_k^2 \rangle = \sigma_k^2$) ^a
i	0	0
T_1	1	Log Uniform
α	0	3/4
$\Delta F_V(\lambda)$	$N_\lambda \times N_{\text{telescopes}}$	Log Uniform
$\bar{F}_V(\lambda)$	$N_\lambda \times N_{\text{telescopes}}$	Log Uniform
$\bar{\tau}(\lambda)$ ^b	N_λ	Uniform

Notes. ^a σ_k is defined in equation (13).

^bThe top-hat centroid lag parameter is optional and used as a substitute for CREAM's disc response function parameters T_1 , α , and i if CREAM is run in 'top-hat' mode.

frequency limit to 0.5 cycles per day for the driving light curve, the width of the top-hat response to 2 d, and restricted the time delay to be within (−10)–50 d. The CREAM fits to the continuum and line light curves are shown in Figs 6 and 7, along with the inferred driving light curve. The model yielded a fit that is a reasonable representation of most of the observed features in the light curves with a few exceptions here and there. The U -band light curve, Fig. 6 (panel h), exhibits large error bars due to atmospheric extinction.

The measured lags and their uncertainties are shown in Tables 5 and 7, relative to the V band in the observed frame. Since we are measuring relative to the V band, we therefore need to subtract this continuum lag from other CREAM values in order to compare CREAM lags to those obtained with the ICCF method. We find that the two methods give consistent results to within uncertainties for $H\gamma$, $\text{He II } \lambda 4686$, $\text{He I } \lambda 5876$, and $H\beta$ lags. We interpret the continuum lags obtained with both ICCF and CREAM in terms of the accretion thin-disc model in Section 4.

4 INTER-BAND CONTINUUM LAGS

We investigate the accretion-disc structure in 3C 120 in terms of the standard accretion-disc model (Shakura & Sunyaev 1973). In this model, continuum delays increase with increasing wavelength due to thermal reprocessing, where the hotter inner part of the disc responds to the variable ionizing source before the cooler outer part of the disc. The lag is interpreted as the light traveltime from the ionizing source to the reprocessing site, where it is reprocessed into UV/optical continuum emission. The temperature profile of the accretion disc changes with radius $r = c\tau$ as $T(r) \propto r^{-3/4}$, for a given BH mass M and accretion rate \dot{M} . The wavelength-dependent lags have been detected before in several studies across a wide range of continuum bands (e.g. Cackett et al. 2007; Edelson et al. 2015; Fausnaugh et al. 2016, 2018; Jiang et al. 2017) with statistically significant lag detections, as predicted by the reprocessing model. We use CREAM as described in Section 3.3 to fit a steady-state blackbody disc model to the U , g' , V , r' , i' , and z_s continuum light curves, in order to assess the temperature profile of the disc $T(r)$ in 3C 120, and determine the accretion rate \dot{M} for $M = 6.3 \times 10^7 M_\odot$. The resulting CREAM model best-fitting parameters are presented in Tables 8 and 9. The probability distribution for T_1 is shown in Fig. 8, yielding the best-fitting value of $T_1 = (1.51 \pm 0.10) \times 10^4$ K. This value of T_1 corresponds to $\dot{M} = 0.60 \pm 0.15 M_\odot \text{ yr}^{-1}$ (equation 11) for our measured BH mass $M = 6.3 \times 10^7 M_\odot$, giving $\log(M \dot{M}/M_\odot^2 \text{ yr}^{-1}) = 7.58 \pm 0.11$. We also report an Eddington ratio $\dot{m}_{\text{Edd}} = \dot{M}/\dot{M}_{\text{Edd}} = L/L_{\text{Edd}} = 0.42^{+0.10}_{-0.09}$. The ratio L/L_{Edd} is

influenced by (1) the inclination and (2) the adopted BH mass that is uncertain by 0.4 dex.

4.1 Lag spectrum

We present the CREAM mean delays alongside ICCF measurements for comparison in Table 7, and plotted in Fig. 9. The CREAM lags increase as $\lambda^{4/3}$ since the CREAM model assumes a flat blackbody disc with $T \propto R^{-3/4}$. The ICCF results also show the same trend of rising lag with wavelength, with the exception of the U band. The U band resulted in a longer lag than that would be expected (i.e. larger than the lag between V and g'). This enhanced U lag has been encountered before (e.g. Edelson et al. 2015; Fausnaugh et al. 2016) and is said to be due to the considerable contribution of Balmer continuum and high-order Balmer lines in the U band.

The observed delay spectrum $\tau(\lambda)$ tests the accretion-disc theory. A thin steady-state blackbody accretion disc has $T^4 = 3GM\dot{M}/8\pi\sigma r^3$ and thus with $T \propto hc/k\lambda$ for blackbody emission, the predicted delay spectrum should follow $\tau = r/c \propto (M\dot{M})^{1/3} \lambda^{4/3}$ (Shakura & Sunyaev 1973). More generally, $\tau \propto \lambda^\beta$ corresponds to $T \propto r^{1/\beta}$.

To quantify the lags for a disc reprocessing model, we fit the ICCF lags with a power law of the form

$$\tau(\lambda) = \tau_0 [(\lambda/\lambda_0)^\beta - 1], \quad (14)$$

where λ_0 is the reference wavelength, β is the power-law index that corresponds to the temperature–radius slope $T \propto r^{-\alpha}$, where $\alpha = 1/\beta$, and τ_0 is a normalization factor for measuring the radius of the disc at λ_0 . In Fig. 9, the orange and black curves show fits of this model with $\lambda_0 = 5477 \text{ \AA}$ and β fixed at 4/3 (black) and free to vary (orange). Since there is an error bar on the ICCF V -band lag ($0.00^{+0.13}_{-0.12}$ d), we add a wavelength-independent constant parameter to equation (14). This new parameter allows for a non-zero V -band lag; in other words, we do not force the fit to have a zero lag at V -band wavelength. In doing so, we find best-fitting value of $\tau_0 = 3.51 \pm 0.22$ d from ICCF ($\chi^2/\text{dof} = 8.44$ for $\text{dof} = 4$). When β is allowed to vary, we find values of $\tau_0 = 2.42 \pm 1.11$ d and $\beta = 1.79 \pm 0.62$ from ICCF measurements ($\chi^2/\text{dof} = 10.95$ for $\text{dof} = 3$); see Table 10. Therefore, we discuss the results for fixed $\beta = 4/3$.

We find that the function gives a poor fit to the ICCF lags owing to the excessive U -band lag and potentially excessive r' and i' lags as well. The large ICCF lags are evident from Fig. 9, with lags of i' , z_s being comparable to and larger than that of the high-ionization-state lines such as $\text{He II } \lambda 4686$. Comparing the intercepts to infer the radius of the disc at λ_0 , $\tau_0 = 3.51 \pm 0.22$ d for ICCF lags versus $\tau_0 = 2.26 \pm 0.18$ d for CREAM, implies a radius that is a factor of 1.55 ± 0.16 times larger than that would be expected from the standard thin-disc model. This discrepancy could be due to several different sources: (1) difficulties in the ICCF in measuring the lags due to slightly noisier U light curve ($\text{SNR} = 50$), influence by outliers, or overinfluenced by the observing gap; (2) contamination of the disc continuum emission by H I bound–free continuum emission from the BLR (Korista & Goad 2001; Lawther et al. 2018; Chelouche, Pozo Nuñez & Kaspi 2019; Korista & Goad 2019). This produces a composite delay distribution, with a sharp peak at small lags from the disc continuum and a broader peak with longer delays from the BLR. Evidence for this H I bound–free continuum from BLR is shown by the Balmer jump at 3640 Å and Paschen jump at 8200 Å in the ICCF lag spectrum. We do not account for diffuse continuum (DC) contribution to the measured continuum lags, we leave that here for future work.

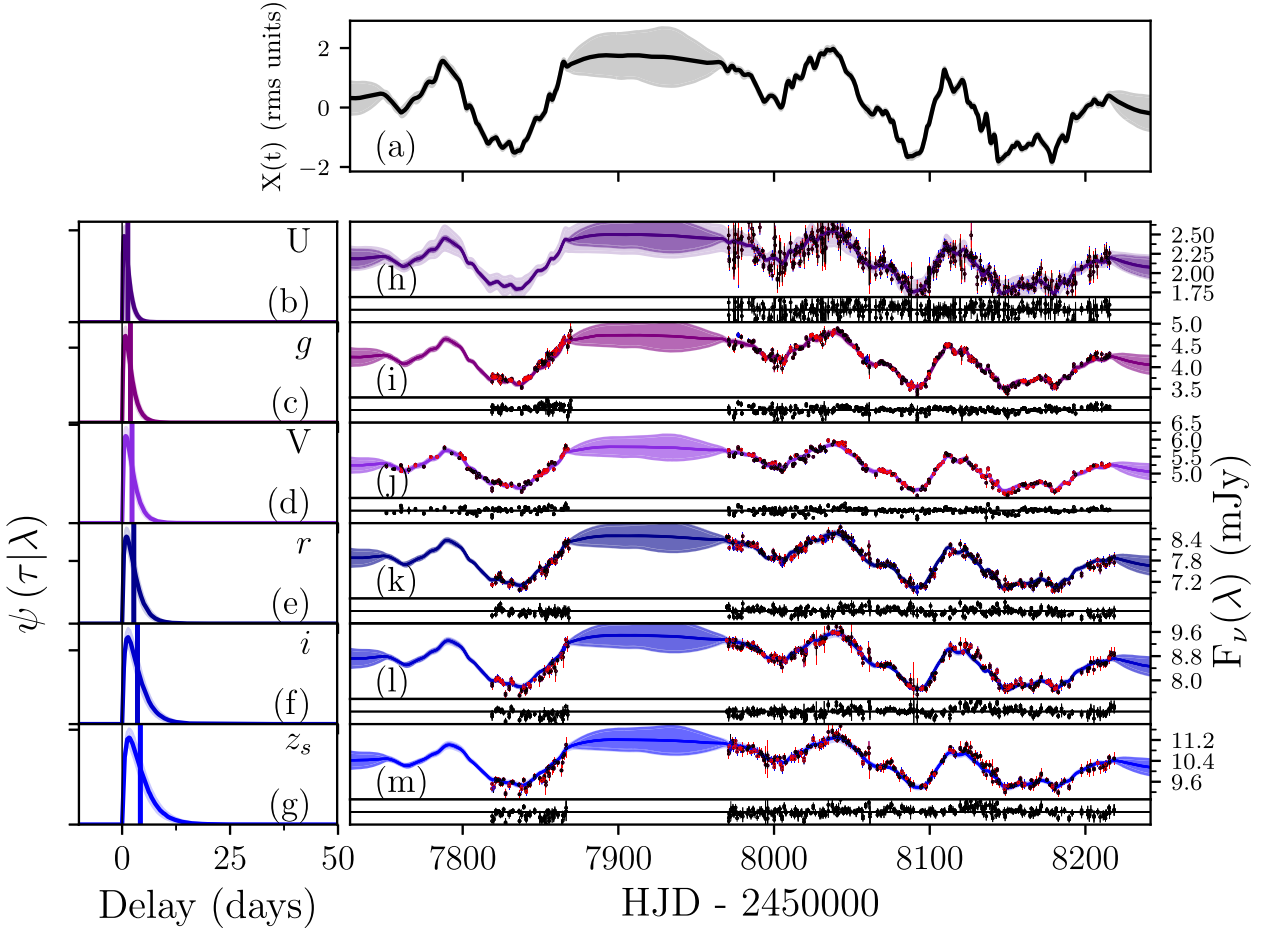


Figure 6. CREAM fits to the continuum light curves (panels h–m) from 3C 120. The upper figure (panel a) shows the inferred driving light curve. Panels b–g show the response functions where the vertical line denotes the mean lags. Also, shown are the fit residuals in panels h–m. The red and blue are the rescaled error bars using equation (8).

4.1.1 Accretion-disc spectrum

The linearized reprocessing model assumes that continuum variations respond linearly to the lampost with a time delay that depends on light-traveltime effects. We see from the CREAM fit shown in Fig. 6 that an approximate linear relation exists between the inferred driver and disc light curves (both experience correlated variations). We explore this further in Fig. 10. The response light curves are plotted relative to the driving light curve $X(t - \tau)$, averaged over the time delay distribution $\Psi(\tau)$ to demonstrate this linear relation. Fig. 10 shows that this relation holds across all continuum bands, indicating that, despite larger than expected delays, a linearized echo description is apparent from correlated variability of these light curves.

In Fig. 11, we plot the rms disc spectrum (variable component of the light) derived from the CREAM fit slopes in Fig. 10 and denoted as $\Delta F_v(\lambda)$ in equation (9) and Table 9. The average (disc+galaxy) spectrum is derived from the CREAM fit intercepts in Fig. 10 and denoted as $\bar{F}_v(\lambda)$. Also shown is the $F_{\max}(\lambda) - F_{\min}(\lambda)$ spectrum corresponding to the difference between maximum and minimum observed fluxes for each wavelength. As a reference, we overplot the fiducial $f_v \propto \nu^{1/3}$ power-law disc spectrum (yellow). From the observed fluxes (dashed lines), it appears that the rms disc spectrum is red rather than blue. We attribute this to extinction and reddening by dust in the Milky Way (MW). We correct for MW extinction

using a dust extinction map (Schlegel, Finkbeiner & Davis 1998) with $E(B - V) = 0.29$ mag and an extinction curve of Fitzpatrick (1999) with $R_V = 3.1$. After correcting for MW dust extinction (solid lines), we can see that the variable disc spectrum is blue and quite close to the $\nu^{1/3}$ spectrum predicted by the thin-disc theory, while the average (disc+galaxy) spectrum remains red. We note that there is no obvious sign in the dust-corrected $\Delta F_v(\lambda)$ or $F_{\max}(\lambda) - F_{\min}(\lambda)$ disc spectrum of Fig. 11 of Balmer or Paschen jumps that might be expected given their signature in delay spectrum $\tau(\lambda)$ of Fig. 9.

We next compare the predicted disc spectrum calculated from the $T(r)$ profile derived from the CREAM fit to $\tau(\lambda)$, with the observed disc spectrum flux. CREAM fit estimates $T(r)$ from $\tau(\lambda)$ (i.e. $M\dot{M}$ from Fig. 8) and independently of that also estimates the disc flux $f_v(\lambda)$ at each wavelength. These are the $\Delta F_v(\lambda)$ and $\bar{F}_v(\lambda)$ in equation (9), which are the slopes and intercepts, respectively, plotted as an (MW-dust-corrected) spectrum in Fig. 11. We want to ascertain if the $T(r)$ from the $M\dot{M}$ in Fig. 8 predicts a disc spectrum $f_v(\lambda)$ that is consistent with (or brighter than, or fainter than) the independently measured disc spectrum in Fig. 11. We make use of equation (4) in Cackett et al. (2007) and equation (2) in Collier et al. (1999) to derive predicted spectra, and compare with the mean disc \bar{F}_{disc} spectrum (red) in Fig. 12, where

$$\bar{F}_{\text{disc}}(\lambda) = \bar{F}(\lambda) - F_{\text{gal}}(\lambda), \quad (15)$$

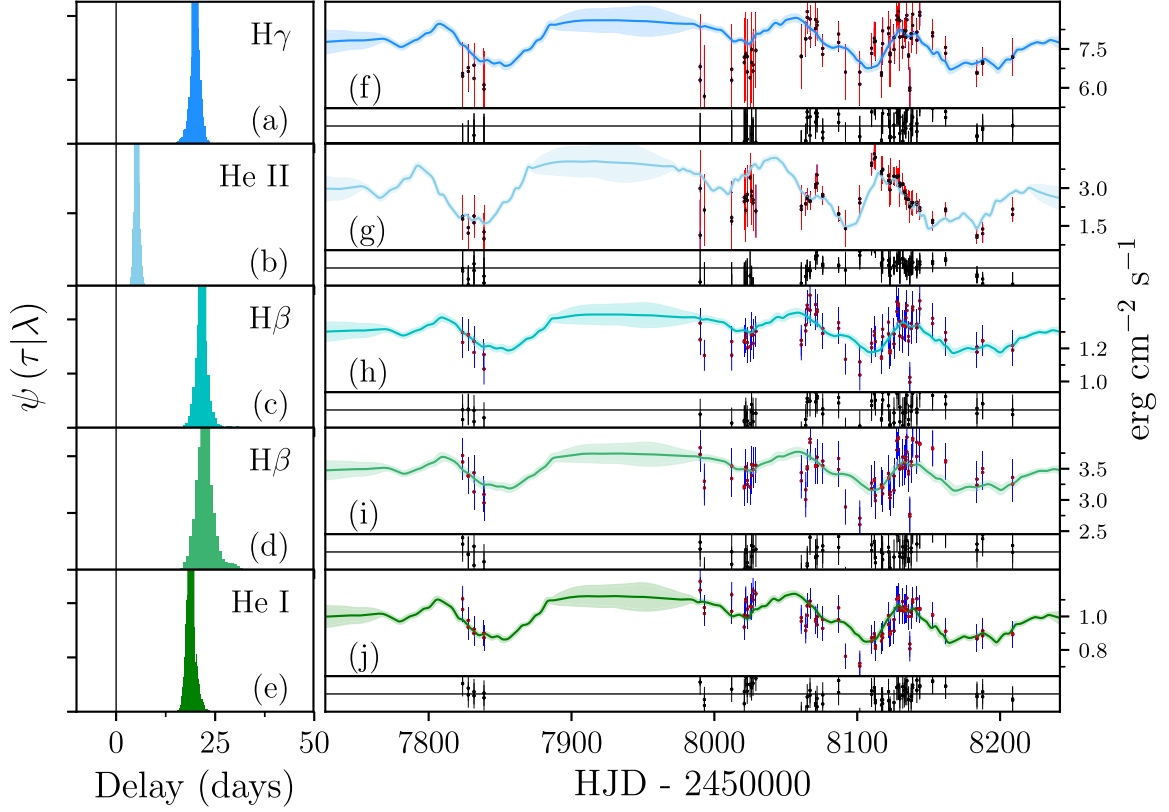


Figure 7. The inferred driving light curve, panel a in Fig. 6, is also fitted to the line light curves (panels f–j). Panels a–e show the posterior delay distributions, defined by CREAM’s MCMC samples of the mean delay of top-hat response functions. The vertical line marks the zero delay. The light curves are H γ λ 4340, He II λ 4686, H β λ 4861 (blue side), H β λ 4861 (red side), and He I λ 5876, respectively. The units are 10^{-13} erg cm $^{-2}$ s $^{-1}$ for H γ and He II, and 10^{-12} erg cm $^{-2}$ s $^{-1}$ for the other panels.

Table 7. 3C 120 continuum lags relative to V in the observed frame.

Line curve	λ (Å)	τ_{cent} (days)	$\tau_{\text{CREAM}} - \tau_V$ (days)	F_{var}
<i>U</i>	3656	$0.14^{+0.35}_{-0.36}$	-0.94 ± 0.21	0.114 ± 0.005
<i>g'</i>	4770	$-0.63^{+0.13}_{-0.13}$	-0.38 ± 0.24	0.092 ± 0.003
<i>V</i>	5477	$0.00^{+0.13}_{-0.12}$	0.00 ± 0.26	0.080 ± 0.002
<i>r'</i>	6231	$1.50^{+0.24}_{-0.24}$	0.42 ± 0.28	0.060 ± 0.002
<i>i'</i>	7625	$2.60^{+0.24}_{-0.24}$	1.25 ± 0.34	0.070 ± 0.002
<i>z_s</i>	8660	$2.86^{+0.24}_{-0.24}$	1.9 ± 0.4	0.059 ± 0.002

Note. $\tau_V = 2.26 \pm 0.18$ d.

Table 8. CREAM model best-fitting parameters.

Parameter	Value
T_1 (10^4 K)	1.51 ± 0.10
i (deg)	0
α	0.75

$$F_{\text{gal}}(\lambda) = \bar{F}(\lambda) + X_{\text{gal}} \Delta F(\lambda). \quad (16)$$

It follows from Fig. 12 that the predicted disc spectrum (for $i = 0$) is brighter by a factor of ~ 4 compared with the \bar{F}_{disc} spectrum. Also, the shape of the \bar{F}_{disc} spectrum is close to $f_\nu \propto \nu^{1/3}$, in agreement with predicted spectrum for a thin steady-state blackbody disc, but

Table 9. Mean and rms spectra from CREAM.

λ (Å)	$\bar{F}_\nu(\lambda)$ (mJy)	$\Delta F_\nu(\lambda)$ (mJy)
3656	7.604 ± 0.011	0.937 ± 0.013
4770	11.308 ± 0.009	0.96 ± 0.01
5477	11.80 ± 0.01	0.92 ± 0.01
6231	15.516 ± 0.013	0.929 ± 0.013
7625	14.317 ± 0.015	0.890 ± 0.013
8660	15.442 ± 0.016	0.817 ± 0.015

Note. The dust-extinction-corrected values.

the surface brightness of the disc is lower by a factor of ~ 4 compared with a face-on blackbody disc with the $T(r)$ profile derived from the delay spectrum $\tau(\lambda)$. This discrepancy is in the same direction as, and somewhat larger than, the result found by Starkey et al. (2017) for the disc in NGC 5548. It suggests that the effect may be more general and not just a peculiarity of NGC 5548.

4.1.2 Optical luminosity at 5100 Å

Using the flux–flux analysis method from CREAM, we determine the optical luminosity at 5100 Å corresponding to our monitoring campaign. A linear relationship is observed between the CREAM-inferred driving light curve (assuming that continuum variations are driven by a central source of irradiation) and all continuum bands. The best-fitting mean flux \bar{F} and rms flux ΔF for each wavelength are listed in Table 9, after correcting for galactic extinction following

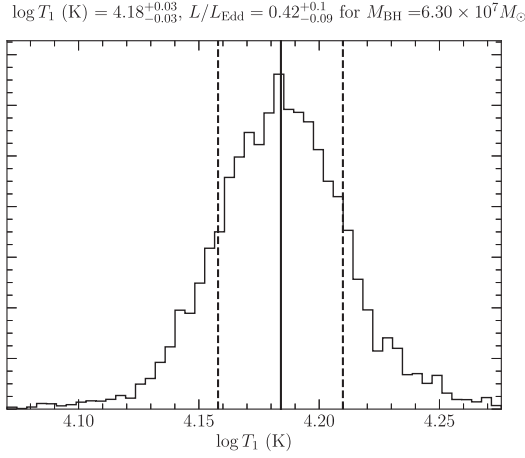


Figure 8. The posterior probability histogram for T_1 as derived by CREAM, for $\alpha = 3/4$ and $i = 0$.

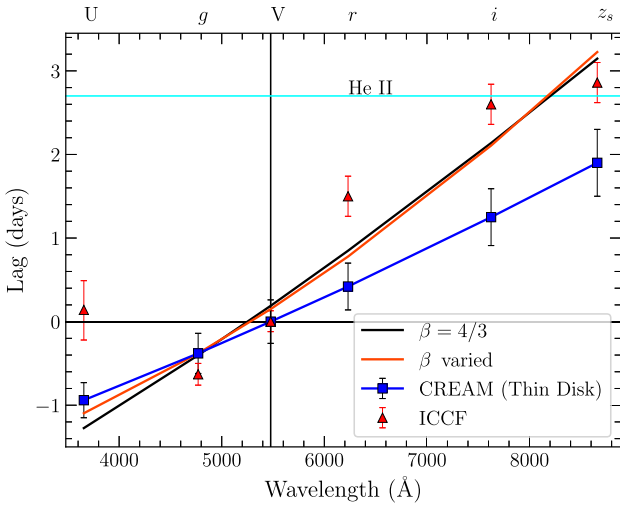


Figure 9. Lag as a function of wavelength relative to the V band (shown by the vertical line). The best fits of τ_0 with $\beta = 4/3$ (black) and β allowed to vary (orange) are shown. The solid blue line is prediction from CREAM standard thin-disc theory with $L/L_{\text{Edd}} = 0.4$. The cyan solid line shows the broad He II emission-line lag of 2.7 d relative to V for comparison.

Table 10. Lag spectrum parameter fits.

Wavelength	τ_0	β	χ^2/dof	dof
All	3.51 ± 0.22	4/3	8.44	4
	2.42 ± 1.11	1.79 ± 0.62	10.95	3

Schlegel et al. (1998). The total flux in each filter includes contributions from the disc and host galaxy. We quantify the galaxy's contribution by evaluating the linear trend lines at $X_{\text{gal}} = -8.12$ for each filter (Fig. 10). The value X_{gal} is defined to be the point where the linear fit extrapolated to low flux first crosses zero. This occurs first at $X_{\text{gal}} = -8.12$, for the fit to the shortest wavelength U-band flux. Table 11 summarizes the results of decomposing total (disc+galaxy) flux into galaxy and disc (total–galaxy) components. We determine the interpolated host-galaxy flux at 5100 Å of $3.913 \pm 0.077 \text{ mJy}$.

Bentz et al. (2006) using high-resolution *HST* images, determined the host-galaxy flux at 5100 Å (5.22 mJy) after correcting for extinction and adding narrow-line contribution (Sakata et al. 2010).

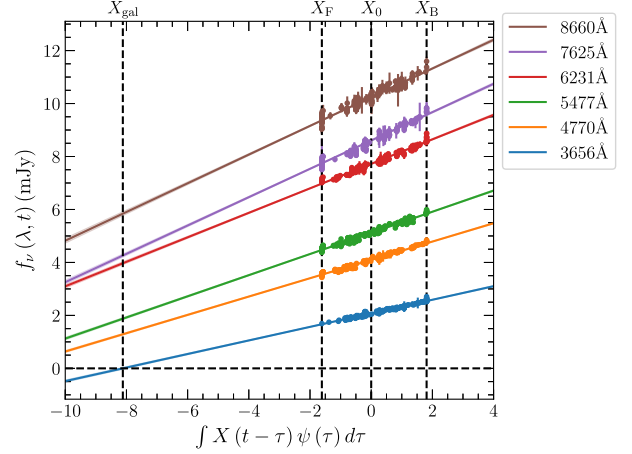


Figure 10. Model response light curves for the CREAM fits to the input light curves (not dust corrected). The vertical lines label the driving light-curve values used to evaluate the galaxy, faint-state, and bright-state spectra (X_{gal} , X_F , X_B). At $X(t) = X_{\text{gal}} = -8.12$, the linear fit crosses zero at the shortest wavelength, placing a lower limit on the host-galaxy flux.

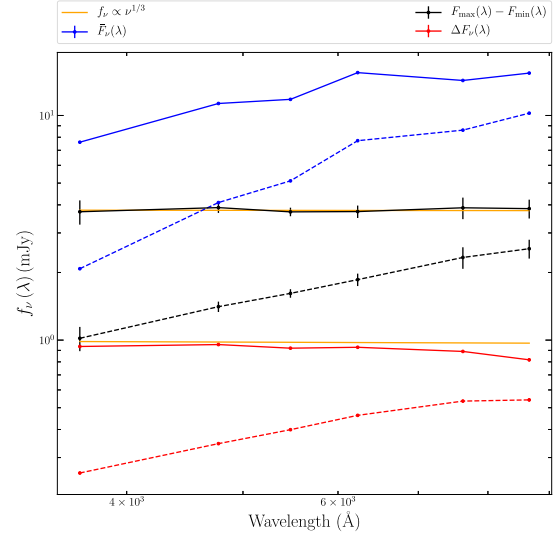


Figure 11. The log–log plot of the mean (disc+galaxy) spectrum (blue), rms disc spectrum (red), and max–min (black) disc spectrum, compared with the expected power-law slope (yellow). The dashed lines correspond to reddened spectra and the solid lines correspond to de-reddened spectra.

Bentz et al. (2009a) re-modelled the host-galaxy flux at 5100 Å and found it to be 3.32 mJy. The difference between these two host-galaxy estimates is linked with the difference in the decomposition modelling techniques of the galaxy (Pozo Nuñez et al. 2012). Through interpolating, we determine the disc (total–galaxy) flux at 5100 Å to be $f_{\text{obs}}[5100 \text{ Å}(1+z)] = 7.55 \pm 0.08 \text{ mJy}$. Using the redshift distance of 139 Mpc, we measure the luminosity at the time of our campaign to be $(9.94 \pm 0.11) \times 10^{43} \text{ erg s}^{-1}$ (Table 12).

5 BH MASS

There have been several previous campaigns (e.g. Peterson et al. 1998b, 2004; Pozo Nuñez et al. 2012; Kollatschny et al. 2014; Grier et al. 2017a; Du et al. 2018b) reporting BH mass estimates in 3C 120. To determine the BH mass, we require the emission-line time delay

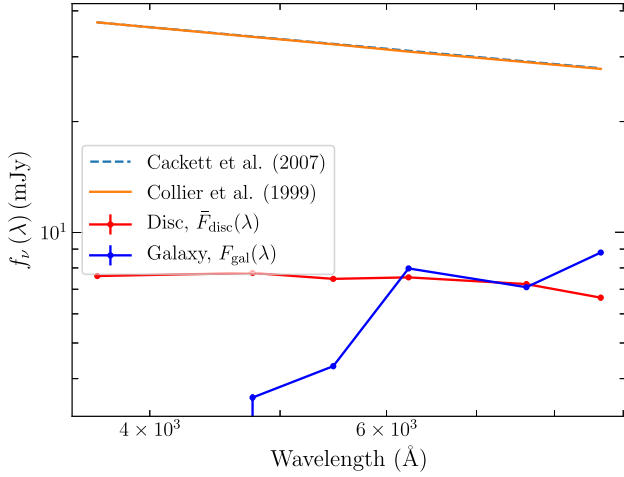


Figure 12. The predicted spectra are shown in blue (dotted) and orange (solid) estimated from the $T(r)$ profile derived from the CREAM fit to $\tau(\lambda)$, compared with the mean disc spectrum shown in red. The host-galaxy spectrum is in blue (solid).

Table 11. Host-galaxy subtracted fluxes for each wavelength (dust corrected).

λ (Å)	Total (mJy)	Galaxy (mJy)	Total–Galaxy (mJy)
3656	7.604 ± 0.011	0	7.604 ± 0.011
4770	11.308 ± 0.009	3.553 ± 0.075	7.75 ± 0.08
5477	11.80 ± 0.01	4.32 ± 0.08	7.47 ± 0.08
6231	15.516 ± 0.013	7.974 ± 0.105	7.54 ± 0.11
7625	14.317 ± 0.015	7.089 ± 0.105	7.23 ± 0.11
8660	15.442 ± 0.016	8.806 ± 0.119	6.64 ± 0.12

τ and velocity width ΔV . Combining these two parameters, we can estimate the mass of the BH using equation (1), thus assuming that the gas motions in the BLR are dominated by the strong gravity of the central BH.

We measure the velocity width and its uncertainty from the mean and rms spectra produced by PrepSpec (Section 2.3). Our linewidth measurements are listed in Table 4. Our measurements are generally consistent with those measured by Kollatschny et al. (2014) but with better statistical errors. We compare only with Kollatschny et al. (2014) because other papers report linewidths only for H β .

We use the velocity dispersion σ_{line} estimated from the rms spectrum in the calculation of the BH mass since it yields less-biased BH mass measurements than FWHM (Peterson 2011). The dimensionless factor f in equation (1) is different for each AGN. For comparison with similar studies on 3C 120, we adopt a mean factor of $\langle f \rangle = 5.5$ (Onken et al. 2004) estimated by bringing the $M_{\text{BH}}-\sigma_*$ relation into agreement with the same relation for quiescent galaxies. We also use our H β lag of $21.2^{+1.6}_{-1.0}$ d relative to the V-band continuum and linewidth ($\sigma_{\text{line}} = 1657 \pm 3 \text{ km s}^{-1}$), to calculate the BH mass. We measured our resulting mass of 3C 120 to be $M = (6.3^{+0.5}_{-0.3}) \times 10^7 (f/5.5) M_{\odot}$.

We compare our BH mass estimate based on H β with the individual campaigns where the H β line was used to measure BH mass in 3C 120 (Table 12 and Fig. 13). Peterson et al. (2004) did a reanalysis of 3C 120 data and reported the H β lag of $39.4^{+22.1}_{-15.8}$ d with a large uncertainty, accounting for the large errors

on their derived BH mass of $M = (5.55^{+3.14}_{-2.25}) \times 10^7 (f/5.5) M_{\odot}$. Grier et al. (2012) deduced a lag of $27.2^{+1.1}_{-1.1}$ d from JAVELIN, which performs better statistically especially on well-sampled data as in their campaign. Hence, the smaller uncertainties led to a BH mass of $M = (6.7^{+0.6}_{-0.6}) \times 10^7 (f/5.5) M_{\odot}$. Recently, Du et al. (2018b) detected a lag of $20.2^{+5.0}_{-4.2}$ d that is similar to our H β lag in this work, and measured the BH mass $[M = (3.26^{+0.83}_{-0.71}) \times 10^7 (f/4.47) M_{\odot}]$. We combine the mass estimates and uncertainties from all measurements to produce the weighted mean (Barlow 2003) of the BH mass $[M = (6.2^{+0.3}_{-0.3}) \times 10^7 (f/5.5) M_{\odot}]$. We note that these BH mass measurements incorporate only the measurement uncertainties in τ and σ_{line} ; they do not take into account the uncertainty in f . We intentionally did not include Peterson et al. (1998b) as no uncertainties were determined on their BH mass. Generally, we find consistent mass estimates to within 1σ error limits except for Du et al. (2018b), possibly due to the significant difference in the H β linewidth and lag they measure compared to other studies since the BH mass is a combination of these two parameters. We also plot the measured H β lags and rms linewidth in Fig. 13 and see that they are generally consistent with the virial assumption (i.e. the lags should decrease as the linewidth increases).

Grier et al. (2017a) measured the BH mass for 3C 120 to be $M = 6.92^{+1.38}_{-1.55} \times 10^7 M_{\odot}$, through dynamical modelling (Pancoast, Brewer & Treu 2014a; Pancoast et al. 2014b) of the object’s BLR. This way of measuring the mass does not assume a particular value of f and relies on direct modelling to measure the BH mass. It also eliminates the uncertainty introduced by assuming a value of f . Using mass derived from dynamical modelling, the virial factor f can be inferred for individual objects. Grier et al. (2017a) estimate f specific to 3C 120 of $f_{\sigma} = 5.75 \pm 2.25$ and $f_{\text{FWHM}} = 6.46 \pm 2.53$, where σ is from the rms spectrum and FWHM is measured from the Grier et al. (2012) mean spectrum. The f adopted here is consistent with f inferred from dynamical modelling, leading to consistent BH masses to within 1σ .

6 VELOCITY-RESOLVED LAG MEASUREMENTS

The ultimate goal of RM studies is to ascertain the geometry and kinematics of the BLR through mapping the responsivity of the line-emitting gas as a function of time lag and line-of-sight velocity. Well-conducted velocity-resolved studies can provide information about the distribution and velocity field of the emitting gas within the BLR, whether infall/inflow, outflow, and/or Keplerian orbits. In an infall/inflow, longer lags are blueshifted having negative velocities and shorter lags are redshifted having positive velocities. In an outflow, the opposite pattern to that of an infall can be seen. Keplerian/circular orbits are symmetric about zero velocity, with shorter lags on the wings of the profile (e.g. Welsh & Horne 1991; Bentz et al. 2009b; Denney et al. 2009b, 2010; Barth et al. 2011; Grier et al. 2013; Du et al. 2016; De Rosa et al. 2018).

We undertook velocity-resolved lag measurements across the H β emission-line profile in 3C 120. Previous studies (Grier et al. 2013, 2017a; Du et al. 2018b) have been successful in recovering the structure and kinematics of the BLR in 3C 120 using velocity-resolved lag measurements. We divided the H β emission-line profile into 11 velocity bins across the line in the continuum-subtracted spectra from -4000 to 4000 km s^{-1} , using the FTN blue-side data. We set the zero velocity using the wavelength of the H β line in rest frame to separate the blueshifted and redshifted measurements. We

Table 12. Outcomes of previous RM studies on 3C 120.

Study	Campaign	H β lag (days)	σ_{line} (km s $^{-1}$)	$M_{\text{BH}}^{(b)}$ ($10^7 M_{\odot}$)	$\log \lambda L_{\lambda}(5100 \text{ \AA})$ (erg s $^{-1}$)
(1)	1989–1996	$39.4^{+22.1}_{-15.8}$	1166 ± 50	$5.55^{+3.14}_{-2.25}$	44.01 ± 0.05
(2)	2008–2009	$27.9^{+7.1}_{-5.9}$	1689 ± 68	$8.5^{+2.3}_{-1.9}$	44.12 ± 0.07
(3)	2009–2010	$23.6^{+1.7}_{-1.7}$	1504 ^(c)	$5.7^{+2.7}_{-2.7}$	43.84 ± 0.04
(4)	2010–2011	$27.2^{+1.1}_{-1.1}$	1514 ± 65	$6.7^{+0.6}_{-0.6}$	43.96 ± 0.06
(5)	2016–2017	$20.2^{+5.0}_{-4.2}$	1360 ± 42	$4.01^{+1.02}_{-0.87}$	$43.99 \pm 0.01^{\text{d}}$
(6)	2016–2018	$21.2^{+1.6}_{-1.0}$	1657 ± 3	$6.3^{+0.5}_{-0.3}$	43.99 ± 0.01
Mean ^(a)				$6.2^{+0.3}_{-0.3}$	

Notes. (1) Peterson et al. (2004); (2) Kollatschny et al. (2014); (3) Pozo Nuñez et al. (2012); (4) Grier et al. (2012); (5) Du et al. (2018b); (6) this work.

^aWeighted average.

^b M masses calculated using $\langle f \rangle = 5.5$ for comparison.

^cMeasured from single-epoch spectra.

^dThe authors do not provide the measurement; we put that here because the two campaigns overlap.

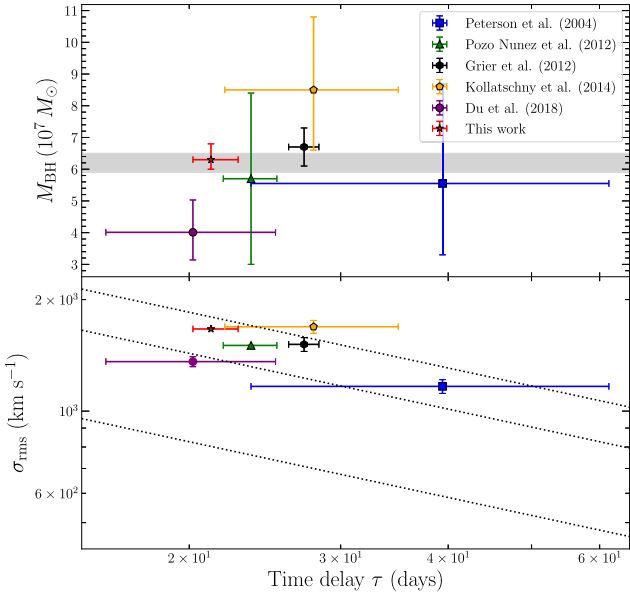


Figure 13. Top: The BH mass as a function of the H β time delay; shown are the different campaigns on 3C 120. The grey band indicates the 1σ envelope of the weighted average of the BH mass based on H β measurements. Bottom: The H β broad emission-line width as a function of the lag. From bottom to top, the dotted lines correspond to constant BH masses of 2×10^7 , 6×10^7 , $1 \times 10^8 M_{\odot}$, respectively, for $f = 5.5$.

constructed H β light curves by integrating the line fluxes in each velocity bin.

We then measured the time lag (τ_{cen}) for each of the light curves with respect to the V-band continuum light curve using the ICCF, as in Section 3.2. We present our velocity-resolved results in the rest frame in Fig. 14 based on the mean spectrum. Our H β velocity-resolved lag profile exhibits a pattern consistent with Keplerian/circular with longer lags at about zero velocity and shorter lags on the wings of the profile. The lag is $\tau \sim 25$ d near line centre and drops symmetrically to ~ 17 d at ± 4000 km s $^{-1}$. This is consistent with Grier et al. (2013) where they deduced a similar morphology.

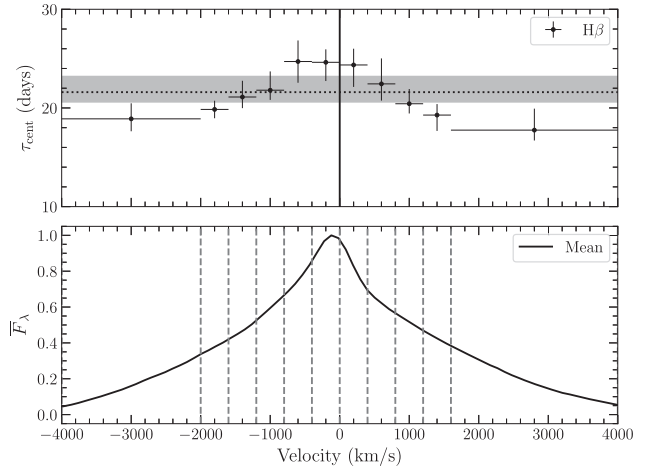


Figure 14. Velocity-resolved lags for the broad H β emission line in 3C 120. The upper panel shows the measured centroid lags at different velocity bins. The dotted horizontal line is the average lag and the grey band its uncertainty (from Table 5). The lower panel shows the continuum-subtracted normalized mean spectrum. The dotted lines show the bins. Error bars in the horizontal direction represent the velocity bin size.

7 DISCUSSION

7.1 Mass determination

Because of its nature, 3C 120 has been the subject of five previous spectroscopic RM studies, thus providing a good sample of independent measurements in the literature to which we compare our results. Based on the ICCF and CREAM methods, we measure the lags of H γ , He II $\lambda 4686$, H β , and He I $\lambda 5876$ in 3C 120 (Table 5). We find that both methods give consistent lag measurements and small uncertainties. We therefore adopt lags from ICCF as our primary method.

We list the variability amplitudes for each of the broad emission lines in Table 5. He II $\lambda 4686$ has a higher variability (30 per cent) and shorter time delay (2 d) than do the Balmer and He I lines, suggesting that it originates really close, within a few light days, of the ionizing source. This may also be an indication of the BLR stratification in 3C 120 (Kollatschny 2003). We compare our measurements with Kollatschny et al. (2014), in which multiple-line lag measurements were also reported. We note that He II $\lambda 4686$ lag is similar to V-band

Table 13. BH masses for the individual lines.

Line	τ (days)	σ_{rms} (km s ⁻¹)	M (M _⊙)
(1)	(2)	(3)	(4)
H γ	18.8 ^{+1.3} _{-1.0}	1786 ± 3	6.4 ^{+0.3} _{-0.5}
He II λ 4686	5.0 ^{+0.8} _{-0.8}	2282 ± 2	2.8 ^{+0.5} _{-0.5}
H β	21.2 ^{+1.6} _{-1.0}	1657 ± 3	6.3 ^{+0.5} _{-0.3}
He I λ 5876	16.9 ^{+0.9} _{-1.1}	2037 ± 12	7.5 ^{+0.4} _{-0.5}
			× 10 ⁷

Note. $\langle f \rangle = 5.5$

lag, suggesting that the He II λ 4686-emitting region is close to V-emitting region (similar physical size). So we add back the V-band continuum lag to He II λ 4686 for comparison with other lines; thus, we end up with 5.0^{+0.8}_{-0.8} d.

Our H β measurement, combined with the previous studies, indicates that the H β line time lag is decreasing since the first campaign (Table 12). Peterson et al. (2004) measured a long delay of 40 ± 20 d. Campaigns succeeding that measured shorter delays with much improved error estimates as a result of robust time delay measurement techniques such as JAVELIN in Grier et al. (2012) and better sampling. This decreasing trend in H β lag might be expected to correspond to a corresponding decrease in optical luminosity. The H β reverberations depend on the continuum level during the time of the monitoring campaign, such that longer time lags would correspond to higher continuum states (Cackett & Horne 2006). This expected correlation is not observed (Table 12).

Using the measured centroid lags of the Helium and Balmer lines, and their rms linewidths, we estimate BH mass from each line, as listed in Table 13. We generally find that the BH masses based on the individual lines are consistent to within 1 σ uncertainties except for He II λ 4686. The BH mass is the combination of the lag and velocity width. The rms spectrum in Fig. 3 shows that the red wing of He II λ 4686 is blended with the H β line, and this blending may lead to underestimation of the linewidth, and hence would affect the final BH mass measurement.

7.2 BLR geometry and kinematics

Our high S/N and high cadence allowed us to carry out the velocity-resolved time lag analysis to probe the geometry and kinematics of the BLR in 3C 120 across the H β emission-line profile. Our velocity-resolved profile is shown in Fig. 14. We see clearly a symmetric pattern about zero velocity consistent with Keplerian motions from -4000 to +4000 km s⁻¹, with higher lags at about zero velocity and shorter lags on the wings. The line wings have almost identical delays with respect to the V-band continuum. This is interesting as it indicates that the velocity field is not dominated by radial inflow or outflow. There is an overall gravitational domination of the BLR gas motions by the BH, thus validating the assumption (i.e. gravity-dominated system) that allows us to measure the mass of the central BH.

Grier et al. (2013) also deduced a kinematics consistent with our findings but with an additional component, in which they interpreted their velocity-resolved lag measurement as a combination of circular orbits plus inflowing gas from the campaign 2010–2011. In an earlier campaign (2008–2009), Kollatschny et al. (2014) deduced a two-component BLR structure similar to that of Grier et al. (2013; 2017a). This is not surprising given the small time gap between

these campaigns. The most recent campaign (2016–2017) is by Du et al. (2018b) in which they deduced from their H β velocity-resolved profile, a pattern consistent with an outflow from -1500 to 1500 km s⁻¹ in their rms spectrum, although with large error bars.

7.3 CREAM thin-disc model

In addition to the broad emission-line variability studies, we also undertook the inter-band continuum variability studies in 3C 120 following our high S/N, densely sampled and highly correlated continuum light curves in six bands spanning the wavelength range from 3656 to 8660 Å. To further investigate this waveband correlation in terms of the standard thin-disc model, we fit the continuum light curves using CREAM’s thin steady-state blackbody disc model [$T = T_1(r_1/r)^{3/4}$ with $T_1^4 \propto M \dot{M}/r_1^3$], in order to measure the disc temperature T_1 at $r = 1$ light day, and hence \dot{M} for $M = 6.3 \times 10^7 M_\odot$. Generally, the CREAM model fits the data quite well even with the sporadic variability in the broad lines. We find values of $T_1 = (1.51 \pm 0.10) \times 10^4$ K, mass accretion rate $\dot{M} = 0.60 \pm 0.15 M_\odot \text{ yr}^{-1}$, and corresponding Eddington ratio $\dot{m}_{\text{Edd}} = \dot{M}/\dot{M}_{\text{Edd}} = L_{\text{bol}}/L_{\text{Edd}} = 0.42^{+0.10}_{-0.09}$, implying that 3C 120 is accreting at about half the Eddington rate. Section 7.3.1 summarizes the results of the CREAM mean delays when compared with model-independent ICCF delays in terms of the τ - λ relation. Section 7.3.2 goes over the accretion-disc spectrum and implications thereof.

7.3.1 Lag spectrum

The ICCF lag spectrum shows lag-wavelength dependence relation consistent with reprocessing model $\tau \propto \lambda^\beta$, when allowing the normalization factor τ_0 to vary and fixing β to 4/3. The excess U lag (i.e. greater than that expected from extrapolating the longer wavelength lags) is observed in Fig. 9. The larger U lag than that would be expected has been reported in previous inter-band continuum lag studies. For example, Edelson et al. (2015) and Fausnaugh et al. (2016) also detect this excess U lag, and link it to contamination by the broad emission lines and DC from the BLR (e.g. Korista & Goad 2001). This DC contamination is signified by the Balmer jump at 3640 Å and Paschen jump at 8200 Å in Fig. 9. This contamination tends to lead to disc sizes several times larger than those expected from standard accretion thin-disc model (e.g. Fausnaugh et al. 2016; McHardy et al. 2018). In our analysis, we find the excess U -band lag (Fig. 9), but with no corresponding excess U band (Fig. 11). If we compare ICCF’s best-fitting disc normalization τ_0 at λ_0 with CREAM, then it results in τ_0 that is a factor of 1.6 times larger, consistent with previous studies in which larger than expected values have been measured.

7.3.2 Accretion-disc spectrum

Using CREAM’s flux-flux method (Starkey et al. 2017), we investigate the origin of the UV/optical continuum variability. In Fig. 10, we observe linear relations with no significant curvature that would indicate a change in shape by the variable component across all the continuum light curves. This strong linear relationship implies that the variable component has a constant flux distribution (Winkler 1997), consistent with a disc reprocessing model. The slopes ΔF_ν of the best-fitting line of $f_\nu(\lambda, t)$ versus $X(t)$ give the spectrum of the variable component. We see that the spectral energy distribution (SED) of the variable spectrum resembles the $f_\nu \propto \lambda^{-1/3}$ spectrum

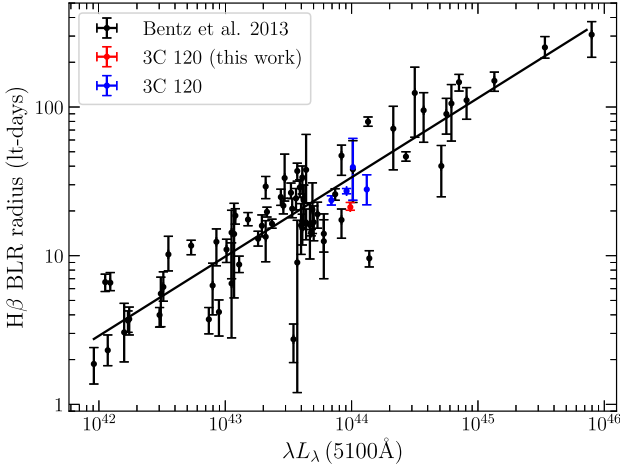


Figure 15. Optical continuum luminosity and $H\beta$ lags for 3C 120 (this work) and other AGNs from Bentz et al. (2013).

expected for a steady-state blackbody accretion disc, after correcting for MW dust extinction. The intercepts \bar{F}_v of the best-fitting line are used to derive the host-galaxy spectrum. We see that the variable component spectrum, after correcting for MW dust extinction, is very close to the $f_\nu \propto \nu^{1/3}$ spectrum predicted by standard thin-disc reprocessing model.

In Fig. 12, we draw the comparison between the observed mean accretion-disc fluxes $f_\nu(\lambda)$ and a predicted blackbody accretion-disc spectrum for a face-on disc, using CREAM fit estimates in Fig. 8. Our finding of a similarly low disc surface brightness in 3C 120 as was found previously for NGC 5548 (Starkey et al. 2017) suggests that this anomaly may be more widespread. We encourage similar analysis to measure both the disc flux and lag spectra in other targets, rather than focusing exclusively on the ICCF delay spectrum.

7.4 Size–luminosity relation

Fig. 15 examines the location of our $H\beta$ lag measurement in the context of the $R_{\text{BLR}}-L$ relationship. We use CREAM’s flux–flux analysis to determine the optical luminosity at 5100 Å corresponding to our campaign, in a similar manner as, e.g. Winkler (1997) and Pozo Nuñez et al. (2012). This led to $\lambda L_\lambda(5100 \text{ Å}) = 10^{43.99 \pm 0.01} \text{ erg s}^{-1}$ after subtracting host-galaxy contribution estimated from Table 11. Fig. 15 shows measurements of the size of the $H\beta$ -emitting region as a function of the optical luminosity at 5100 Å using measurements from Bentz et al. (2013). Our measurement is consistent with the general $H\beta$ trend.

7.5 $M_{\text{BH}}-\sigma_*$ relation

We also investigate if 3C 120 obeys the general trend of the scaling relations between M_{BH} and host-galaxy properties. We adopt the stellar velocity dispersion of 3C 120 of $\sigma_* = 162 \pm 20 \text{ km s}^{-1}$ reported in Nelson & Whittle (1995). We provide the $M_{\text{BH}}-\sigma_*$ relation combining the samples of McConnell & Ma (2013) for inactive galaxies, and the reverberation-mapped AGN sample of Woo et al. (2010), along with our measurement of 3C 120 in Fig. 16. The best-fitting lines are characterized by

$$\log(M_{\text{BH}}/M_\odot) = \alpha + \beta \log(\sigma_*/200 \text{ km s}^{-1}). \quad (17)$$

For a sample of reverberation masses, Woo et al. (2010) measured $\alpha = 8.00 \pm 0.24$ and $\beta = 3.55 \pm 0.60$ assuming $\log f = 0.72 \pm 0.10$

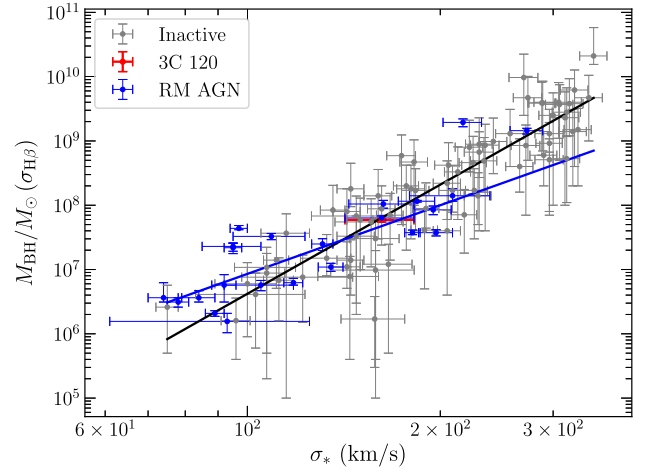


Figure 16. $M_{\text{BH}}-\sigma_*$ relation of inactive galaxy sample (grey), compared with active galaxies with reverberation masses (blue). The reverberation masses were measured using a virial factor of $f = 5.2$. The solid lines are the best-fitting lines to the reverberation sample ($\alpha = 8.00$ and $\beta = 3.55$) and inactive galaxy sample ($\alpha = 8.32$ and $\beta = 5.64$).

with the intrinsic scatter of $\sigma_{\text{int}} = 0.43 \pm 0.08$ dex. McConnell & Ma (2013) measured $\alpha = 8.32 \pm 0.05$ and $\beta = 5.64 \pm 0.32$ for a sample of 72 quiescent galaxies. In both cases, we find that our target shows no significant deviation from the $M_{\text{BH}}-\sigma_*$ relation for quiescent galaxies and reverberation-based samples.

8 CONCLUSION

We carried out fully robotic photometric and spectroscopic observations of the well-studied broad-line radio galaxy 3C 120 with the LCO from 2016 December to 2018 April as part of the LCO AGN Key Project on Reverberation Mapping of Accretion Flows. We summarize the main results as follows:

- (i) We used the ICCF method alongside CREAM to carry out multiple-line ($H\gamma$, $\text{He II } \lambda 4686$, $H\beta$, $\text{He I } \lambda 5876$) lag measurements in 3C 120. We find that the two techniques give consistent results to within uncertainties.
- (ii) We find lags relative to V of 2.7 d for He II and 15–18 d for He I and Balmer lines, consistent with a decrease in ionization with radius.
- (iii) Combining the $H\beta$ lag ($21.2^{+1.6}_{-1.0}$ d) relative to V , and its velocity dispersion ($\sigma_{\text{line}} = 1657 \pm 3 \text{ km s}^{-1}$) in the rms spectrum, we infer a central BH mass ($6.3^{+0.5}_{-0.3} \times 10^7 M_\odot$) that is in accord with results from previous studies after correcting to a common virial correction factor $f = 5.5$.
- (iv) From our velocity-resolved $H\beta$ lag measurements, we deduced a symmetric pattern with a 25 d lag at line centre reducing to ~ 17 d on both the blue and red wings of the line.
- (v) Our inter-band continuum variability study reveals wavelength-dependent delays with longer delays at longer wavelengths. The delays span 3–4 d, and are compatible with $\tau \propto \lambda^{4/3}$ apart from an excess of 1 or 2 d in the U band.
- (vi) Our CREAM analysis, fitting a face-on reverberating steady-state blackbody disc model, finds $M M_\odot = 10^{7.58 \pm 0.11} M_\odot \text{ yr}^{-1}$ corresponding to $L/L_{\text{Edd}} \sim 0.4$ for $M = 6.3 \times 10^7 M_\odot$.
- (vii) We measure the size of the disc to be 1.6 times larger than the prediction from CREAM thin-disc theory with $L/L_{\text{Edd}} \sim 0.4$, consistent with other RM continuum studies.

(viii) The SED of the disc spectrum, isolated by variations, matches $F_\nu \propto \nu^{1/3}$ from disc theory with no sign of bound-free edges.

The CREAM thin-disc model generally fits the 3C 120 data relatively well. In the future, we want to explore departures from the thin-disc model by varying the inclination (from face-on), the power index α to see how it affects the mass accretion rate in 3C 120, and potentially the Eddington ratio in terms of the thin-disc theory. Due to the high quality of these observations, they lend themselves to potential further study for a more detailed model for 3C 120.

ACKNOWLEDGEMENTS

MH and ERC acknowledge support from the South African National Research Foundation (NRF). KH acknowledges support from STFC grant ST/R000824/1. MH and SMC were supported in part by the Space Telescope Science Institute (STScI) Director's Discretionary Research Fund (DDRF). Research by AJB was supported by NSF grants AST-1412693 and AST-1907290. Research by DJS is supported by NSF grants AST-1821967, 1821987, 1813708, 1813466, and 1908972. TT acknowledges support by the NSF through grants AST-1412315 and AST-1907208 and by the Packard Foundation through a Packard Fellowship.

DATA AVAILABILITY

The data underlying this article are available in the article and its online supplementary material.

REFERENCES

Antonucci R., 1993, *ARA&A*, 31, 473
 Barlow R., 2003, in Lyons L., Mount R., Reitmeyer R., eds, Proc. PHY-STAT2003, Statistical Problems in Particle Physics, Astrophysics, and Cosmology. p. 250
 Barth A. J. et al., 2011, *ApJ*, 743, L4
 Barth A. J. et al., 2015, *ApJS*, 217, 26
 Bentz M. C., Katz S., 2015, *PASP*, 127, 67
 Bentz M. C., Peterson B. M., Pogge R. W., Vestergaard M., Onken C. A., 2006, *ApJ*, 644, 133
 Bentz M. C., Peterson B. M., Netzer H., Pogge R. W., Vestergaard M., 2009a, *ApJ*, 697, 160
 Bentz M. C. et al., 2009b, *ApJ*, 705, 199
 Bentz M. C. et al., 2013, *ApJ*, 767, 149
 Blandford R. D., McKee C. F., 1982, *ApJ*, 255, 419
 Blanton M. R., Roweis S., 2007, *AJ*, 133, 734
 Brown T. M. et al., 2013, *PASP*, 125, 1031
 Cackett E. M., Horne K., 2006, *MNRAS*, 365, 1180
 Cackett E. M., Horne K., Winkler H., 2007, *MNRAS*, 380, 669
 Chambers K. C. et al., 2016, preprint (arXiv:1612.05560)
 Chelouche D., Pozo Nuñez F., Kaspi S., 2019, *Nat. Astron.*, 3, 251
 Collier S., Horne K., Wanders I., Peterson B. M., 1999, *MNRAS*, 302, L24
 Collins K. A., Kielkopf J. F., Stassun K. G., Hessman F. V., 2017, *AJ*, 153, 77
 De Rosa G. et al., 2018, *ApJ*, 866, 133
 Denney K. D., Peterson B. M., Dietrich M., Vestergaard M., Bentz M. C., 2009a, *ApJ*, 692, 246
 Denney K. D. et al., 2009b, *ApJ*, 704, L80
 Denney K. D. et al., 2010, *ApJ*, 721, 715
 Du P. et al., 2016, *ApJ*, 820, 27
 Du P. et al., 2018a, *ApJ*, 856, 6
 Du P. et al., 2018b, *ApJ*, 869, 142
 Ducati J. R., Bevilacqua C. M., Rembold S. r. B., Ribeiro D., 2001, *ApJ*, 558, 309

Edelson R. A., Krolik J. H., 1988, *ApJ*, 333, 646
 Edelson R., Turner T. J., Pounds K., Vaughan S., Markowitz A., Marshall H., Dobbie P., Warwick R., 2002, *ApJ*, 568, 610
 Edelson R. et al., 2015, *ApJ*, 806, 129
 Fausnaugh M. M. et al., 2016, *ApJ*, 821, 56
 Fausnaugh M. M. et al., 2017, *ApJ*, 840, 97
 Fausnaugh M. M. et al., 2018, *ApJ*, 854, 107
 Ferrarese L., Ford H., 2005, *Space Sci. Rev.*, 116, 523
 Ferrarese L., Merritt D., 2000, *ApJ*, 539, L9
 Fitzgerald M. P., 1970, *A&A*, 4, 234
 Fitzpatrick E. L., 1999, *PASP*, 111, 63
 Gaskell C. M., Peterson B. M., 1987, *ApJS*, 65, 1
 Gaskell C. M., Sparke L. S., 1986, *ApJ*, 305, 175
 Gebhardt K. et al., 2000, *ApJ*, 539, L13
 Gómez J. L., Roca-Sogorb M., Agudo I., Marscher A. P., Jorstad S. G., 2011, *ApJ*, 733, 11
 Grier C. J. et al., 2012, *ApJ*, 755, 60
 Grier C. J. et al., 2013, *ApJ*, 764, 47
 Grier C. J., Pancoast A., Barth A. J., Fausnaugh M. M., Brewer B. J., Treu T., Peterson B. M., 2017a, *ApJ*, 849, 146
 Grier C. J. et al., 2017b, *ApJ*, 851, 21
 Grier C. J. et al., 2018, *ApJ*, 868, 76
 Henden A. A., Levine S., Terrell D., Welch D. L., 2015, Am. Astron. Soc. Meeting Abstr., 225, 336.16
 Jiang Y.-F. et al., 2017, *ApJ*, 836, 186
 Kaspi S., Smith P. S., Netzer H., Maoz D., Jannuzi B. T., Givon U., 2000, *ApJ*, 533, 631
 Kollatschny W., 2003, *A&A*, 407, 461
 Kollatschny W., Ulbrich K., Zetzl M., Kaspi S., Haas M., 2014, *A&A*, 566, A106
 Korista K. T., Goad M. R., 2001, *ApJ*, 553, 695
 Korista K. T., Goad M. R., 2019, *MNRAS*, 489, 5284
 Kormendy J., Gebhardt K., 2001, in Wheeler J. C., Martel H., eds, AIP Conf. Proc. Vol. 586, 20th Texas Symposium on Relativistic Astrophysics. Am. Inst. Phys., New York, p. 363
 Kormendy J., Richstone D., 1995, *ARA&A*, 33, 581
 Lawther D., Goad M. R., Korista K. T., Ulrich O., Vestergaard M., 2018, *MNRAS*, 481, 533
 Li J. et al., 2017, *ApJ*, 846, 79
 Li Y.-R., Zhang Z.-X., Jin C., Du P., Cui L., Liu X., Wang J.-M., 2020, *ApJ*, 897, 18
 Lynden-Bell D., Rees M. J., 1971, *MNRAS*, 152, 461
 McConnell N. J., Ma C.-P., 2013, *ApJ*, 764, 184
 McHardy I. M. et al., 2018, *MNRAS*, 480, 2881
 Magorrian J. et al., 1998, *AJ*, 115, 2285
 Nelson C. H., Whittle M., 1995, *ApJS*, 99, 67
 Onken C. A., Ferrarese L., Merritt D., Peterson B. M., Pogge R. W., Vestergaard M., Wandel A., 2004, *ApJ*, 615, 645
 Pancoast A., Brewer B. J., Treu T., 2014a, *MNRAS*, 445, 3055
 Pancoast A., Brewer B. J., Treu T., Park D., Barth A. J., Bentz M. C., Woo J.-H., 2014b, *MNRAS*, 445, 3073
 Pauliny-Toth I. I. K., Kellermann K. I., 1966, *ApJ*, 146, 634
 Peterson B. M., 1993, *PASP*, 105, 247
 Peterson B. M., 2001, in Aretxaga I., Kunth D., Mújica R., eds, Advanced Lectures on the Starburst-AGN. World Sci., Singapore, p. 3
 Peterson B. M., 2011, preprint (arXiv:1101.0001)
 Peterson B. M., Wanders I., Horne K., Collier S., Alexander T., Kaspi S., Maoz D., 1998a, *PASP*, 110, 660
 Peterson B. M., Wanders I., Bertram R., Hunley J. F., Pogge R. W., Wagner R. M., 1998b, *ApJ*, 501, 82
 Peterson B. M. et al., 2004, *ApJ*, 613, 682
 Peterson B. M. et al., 2013, *ApJ*, 779, 109
 Pozo Nuñez F., Ramolla M., Westhues C., Bruckmann C., Haas M., Chini R., Steenbrugge K., Murphy M., 2012, *A&A*, 545, A84
 Ramolla M. et al., 2018, *A&A*, 620, A137
 Rodríguez-Pascual P. M. et al., 1997, *ApJS*, 110, 9
 Sakata Y. et al., 2010, *ApJ*, 711, 461
 Sargent W. L. W., 1967, *PASP*, 79, 369

- Schlegel D. J., Finkbeiner D. P., Davis M., 1998, *ApJ*, 500, 525
 Shakura N. I., Sunyaev R. A., 1973, *A&A*, 24, 337
 Shen Y. et al., 2015, *ApJS*, 216, 4
 Shen Y. et al., 2016, *ApJ*, 818, 30
 Starkey D. A., Horne K., Villforth C., 2016, *MNRAS*, 456, 1960
 Starkey D. et al., 2017, *ApJ*, 835, 65
 Sun M., Grier C. J., Peterson B. M., 2018, PyCCF: Python Cross Correlation Function for Reverberation Mapping Studies, Astrophysics Source Code Library, record ascl:1805.032
 Urry C. M., Padovani P., 1995, *PASP*, 107, 803
 Valenti S. et al., 2015, *ApJ*, 813, L36
 van Dokkum P. G., 2001, *PASP*, 113, 1420
 Vestergaard M., 2002, *ApJ*, 571, 733
 Walker R. C., 1997, *ApJ*, 488, 675
 Wandel A., Peterson B. M., Malkan M. A., 1999, *Astron. Nachr.*, 320, 319
 Welsh W. F., 1999, *PASP*, 111, 1347
 Welsh W. F., Horne K., 1991, *ApJ*, 379, 586
 White R. J., Peterson B. M., 1994, *PASP*, 106, 879
 Winkler H., 1997, *MNRAS*, 292, 273
 Woo J.-H. et al., 2010, *ApJ*, 716, 269
 Zhang Z.-X. et al., 2019, *ApJ*, 876, 49
 Zu Y., Kochanek C. S., Peterson B. M., 2011, *ApJ*, 735, 80

SUPPORTING INFORMATION

Supplementary data are available at *MNRAS* online.

Table A1. Continuum light-curve data.

Table A2. Emission-line light-curve data.

Please note: Oxford University Press is not responsible for the content or functionality of any supporting materials supplied by the authors. Any queries (other than missing material) should be directed to the corresponding author for the article.

APPENDIX A: ADDITIONAL TABLES

Table A1. Continuum light-curve data.

HJD – 2450000 (days)	Flux (mJy)	Error (mJy)	Band
7970.851	2.471	0.099	<i>U</i>
7970.855	2.298	0.078	<i>U</i>
7971.278	2.229	0.080	<i>U</i>
7971.282	2.257	0.075	<i>U</i>

Table A1 – *continued*

HJD – 2450000 (days)	Flux (mJy)	Error (mJy)	Band
7974.237	2.469	0.214	<i>U</i>
7818.909	3.871	0.054	<i>g'</i>
7818.911	3.736	0.051	<i>g'</i>
7819.266	3.828	0.032	<i>g'</i>
7819.268	3.752	0.031	<i>g'</i>
7820.265	3.772	0.032	<i>g'</i>
7751.044	5.322	0.017	<i>V</i>
7751.048	5.285	0.014	<i>V</i>
7756.114	5.226	0.013	<i>V</i>
7756.118	5.206	0.013	<i>V</i>
7760.362	5.184	0.017	<i>V</i>
7818.924	7.177	0.078	<i>r'</i>
7818.925	7.190	0.064	<i>r'</i>
7821.276	7.288	0.046	<i>r'</i>
7821.278	7.120	0.045	<i>r'</i>
7822.269	7.272	0.046	<i>r'</i>
7818.927	7.923	0.067	<i>i'</i>
7818.929	7.846	0.067	<i>i'</i>
7821.280	7.946	0.046	<i>i'</i>
7821.282	7.890	0.047	<i>i'</i>
7822.273	7.961	0.045	<i>i'</i>
7818.932	9.356	0.069	<i>z_s</i>
7818.935	9.544	0.066	<i>z_s</i>
7819.971	9.448	0.120	<i>z_s</i>
7819.974	9.393	0.181	<i>z_s</i>
7821.284	9.518	0.049	<i>z_s</i>

Note. The full table is available online.

Table A2. Emission-line light-curve data.

HJD – 2450000 (days)	Flux (10^{-12} erg s $^{-1}$ cm $^{-2}$)	Error (10^{-12} erg s $^{-1}$ cm $^{-2}$)	Light curve
7823.763	1.524	0.026	H γ
7823.785	1.503	0.030	H γ
7827.749	1.579	0.021	H γ
7827.770	1.538	0.022	H γ
7831.756	1.596	0.022	H γ
7823.763	0.360	0.031	He II λ 4686
7823.785	0.330	0.034	He II λ 4686
7827.749	0.203	0.025	He II λ 4686
7827.770	0.269	0.026	He II λ 4686
7831.756	0.313	0.026	He II λ 4686
7823.763	3.140	0.029	H β blue side
7823.785	2.994	0.032	H β blue side
7827.749	3.101	0.026	H β blue side
7827.770	3.085	0.027	H β blue side
7831.756	2.999	0.027	H β blue side
7823.763	4.533	0.025	H β red side
7823.785	4.458	0.027	H β red side
7827.749	4.231	0.022	H β red side
7827.770	4.224	0.024	H β red side
7831.756	4.253	0.024	H β red side
7823.763	1.087	0.016	He I λ 5876
7823.785	1.027	0.017	He I λ 5876
7827.749	0.961	0.014	He I λ 5876
7827.770	0.913	0.015	He I λ 5876
7831.756	0.899	0.015	He I λ 5876

Note. The full table is available online.

This paper has been typeset from a \LaTeX file prepared by the author.